Dry Metal Forming Open Access Journal

Final Project Report

Edited by Frank Vollertsen
Available online at elib.suub.uni-bremen.de

www.drymetalforming.de

Dry Met. Forming OAJ FPR 6 (2020) 128–165
Date of Report 31 May 2020; published 12 Juni 2020

# Tribological system for cold sheet metal forming based on volatile lubricants and laser structured surfaces

**(DFG Grant Li 1556/36&49; GR 3172/14&21; HI 1397/6&9; TO 211/3, Funding Period 01.02.2014-31.01.2021)**

Gerd Reichardt[1*], Christoph Wörz[1], Markus Singer[1], Mathias Liewald[1],

Manuel Henn[2*], Daniel J. Förster[2], Ehsan Zahedi[2], Steffen Boley[2], Anne Feuer[2], Volkher Onuseit[2], Rudolf Weber[2], Thomas Graf[2],

Georg Umlauf[3], Paul Reichle[4*], Jakob Barz[3,4], Günter E.M. Tovar[4], Thomas Hirth[5]

[1]Institute for Metal Forming Technology, University of Stuttgart, Holzgartenstr. 17, 70174 Stuttgart, Germany
[2]Institut für Strahlwerkzeuge, University of Stuttgart, Pfaffenwaldring 43, 70569 Stuttgart, Germany
[3]Fraunhofer Institute for Interfacial Engineering and Biotechnology, Nobelstr. 12, 70569 Stuttgart, Germany
[4]Institute of Interfacial Process Engineering and Plasma Technology, University of Stuttgart, Nobelstr. 12, 70569 Stuttgart, Germany
[5]Karlsruhe Institute of Technology, Kaiserstr. 12, 76131 Karlsruhe, Germany

## Summary

A novel tribological system has been developed, in which volatile lubricants (carbon dioxide - $CO_2$ or nitrogen- $N_2$) are used as a substitute for mineral oil-based lubricants in deep drawing processes. This process enables the introduction of an intermediate medium under high pressure through flow-optimized, laser-drilled micro holes into the contact surfaces. This eliminates the need for subsequent, cost-intensive cleaning processes, as the volatile lubricants evaporate without leaving any residue during expansion to ambient pressure.

The design of initial micro hole geometries was based on simulations of the flow behaviour of the lubricants passing through, which in turn were validated using pressure reactor tests. In addition, the wetting behaviour of $CO_2$ on relevant surfaces (tool surface and sheet material surface) was investigated experimentally using the captive-bubble-method. Thus, the optimal design of the micro holes (diameter, hole geometry and number of micro holes) could be determined using flat strip drawing tests. The optimal micro hole geometry determined in this way is suited for the use of both $CO_2$ and $N_2$ as volatile lubricant. Furthermore, extensive investigations for the production of the required micro hole geometry by laser drilling were carried out. The fundamentals for drilling micro holes in steel with high aspect ratios could be developed using an ultrashort pulsed research laser with very high pulse energy. Further experiments were conducted using an ultrashort pulsed prototype laser of the kW-class specially developed to increase productivity when drilling a multitude of micro holes with higher average laser power. The novel tribological system has been characterised by means of strip drawing tests and stretch bending tests. For both, $CO_{2\,(liquid)}$ and $N_{2\,(gaseous)}$, relatively low friction values could be achieved compared to conventional lubricants. It could be shown that deep drawing with both $CO_2$ and $N_2$ as dry lubricants is possible. Here, usage of the volatile lubricants not only allows the replacement of mineral oil based lubricants, but even improves the tribological system with regard to frictional forces in sheet metal forming. The feasibility of the new tribological system has been proven by performing deep drawing tests of rectangular cups. These tests showed a significantly enlarged process window of the forming process, which emphasise the tremendous potential of this new tribological system.

**Keywords:** Dry Metal Forming, Deep drawing, Ultrashort pulsed laser drilling, volatile Lubricant


*E-mail address of corresponding authors: gerd.reichardt@ifu.uni-stuttgart.de, manuel.henn@ifsw.uni-stuttgart.de, paul.reichle@igvp.uni-stuttgart.de

## 1 Introduction/Background

Since 1992 Mishina [1] investigated the general tribological lubricating properties of various gas atmospheres (dry air, oxygen and nitrogen) and found a dependency between gas type and friction, several groups [2] did research on the effects of the gas atmosphere on friction and wear of the steel–steel contact and determined low coefficients of friction (COF) for $CO_2$. These studies are the reason for focusing on the lubrication with carbon dioxide and nitrogen in this research.

Mineral oil-based lubricants or oil-water emulsions are usually used as intermediate media in sheet metal cold forming processes to reduce friction and wear. However, these lubricants often contain toxic additives and the formed components must be cleaned for further process steps at high costs and in a time-consuming manner [3]. For these reasons, dispensing with conventional lubricants by using novel dry lubricant systems has a positive effect on the environment and the cost-effectiveness of production processes.

In the research project reported about in this contribution, a novel, environmentally friendly lubricant system for sheet metal cold forming has been developed over three funding periods. In this tribo-system, volatile media such as liquid carbon dioxide ($CO_2$) or gaseous nitrogen ($N_2$) are used as temporary acting dry lubricants, principally shown in Fig. 1. The volatile lubricants are introduced under high pressure directly into the friction zones between the workpiece and the tool during the forming process via laser-drilled micro holes.

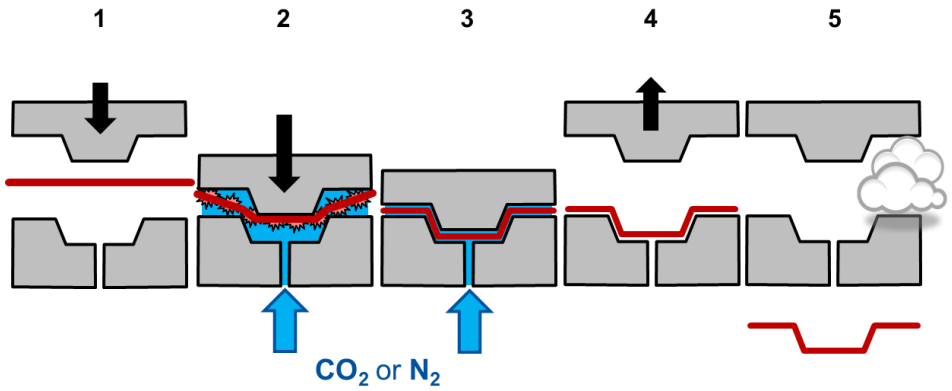


Fig. 1: Working principle of dry deep drawing using volatile media as a lubricant substitute. Adapted from [4].

Fig. 2 shows the successive research objectives of the three funding periods aiming at the realisation of a deep drawing process with volatile lubricants.


Fig. 2: Main aims of the three funding periods to realize dry deep drawing using volatile media as lubrication.

In order to prove the principle function of the novel tribological system, basic friction investigations were conducted initially. For this purpose, numerous flat strip drawing tests were carried out during the first two funding periods, as these tests reproduce the tribological conditions at the component flange, i.e. in the forming zone during deep drawing. For this, the IFU's existing flat strip drawing rig was modified in such a way, that the volatile lubricants could be injected into the contact zone under high pressure (see chapter 5.1). Aim of this was to analyse all relevant factors influencing the friction behaviour of the novel tribological system. The tool radii, which are highly loaded during deep drawing processes, were characterised in the 3rd funding period by using a stretch-bending test (SBT) set up.

The first implementation of the novel tribological system was done in the 2nd funding period on the basis of the deep drawing process of a U-profile and a rectangular cup. For gaining a deeper understanding of the frictional influences, optimising the tools and the process and proving the process stability under near-series conditions, an automated test facility for deep drawing rectangular cups in endurance run was set up.

Before getting into the topic of dry forming with volatile lubrication media, another aspect needs to be discussed: the handling of larger amounts of carbon dioxide and nitrogen. The major constituent of air with almost 80 % (based on the partial pressure) is Nitrogen. This is the reason for escaping $N_2$ to mix very fast with the surrounding air. At room temperature and atmospheric pressure, nitrogen and carbon dioxide are odourless and colourless gases. Both are very common as protection gases in manufacturing because of their low chemical reactivity. $CO_2$ and $N_2$ are non-flammable and therefore used for extinguishing fire. Due to its density of around 1.5 times heavier than dry air at atmospheric conditions (20°C, 1 bar), carbon dioxide is dangerous. Therefore, in the past some fatal accidents happened in cellars, feed silos and mines, because the oxygen was displaced by the $CO_2$. However, only an accumulation of $CO_2$ in poorly ventilated rooms is dangerous. Outdoors or in well-ventilated rooms, the concentration of the escaping carbon dioxide in the air is low, therefore no risk exists. $CO_2$ is not categorically toxic – only in higher concentrations the oxygen delivery for the human body is critical. The short-term lethal dose is around 20 % (based on the partial pressure) of $CO_2$ in the surrounding atmosphere. Therefore, the maximum allowed long-term workplace concentration is 0.5 %. To protect workers from a high $CO_2$ or $N_2$ concentration, ventilation and warning devices are necessary and easily installed.

Another discussion about $CO_2$ is its effect on climate change. Since the industrialization, the naturally occurring concentration of carbon dioxide in the air is rising and currently around 400 ppm. The $CO_2$ used in this research is obtained from the exhaust gas resulting from the combustion of fossil fuels, which leads to no additional emission of $CO_2$ into the environment. Although the world community tries to reduce fossil combustion, there will still be enough processes in the future through which $CO_2$ can be obtained as a by-product. Hence this gas can be seen as a cost-efficient and easily provided lubrication medium.

## 2 Numerical investigations regarding flow behaviour of volatile lubrication media

Calculations for the stability of the tool showed, that 5 mm forming tool thickness is necessary to ensure no mechanical damage of the tool during a normal forming process. Hence, the distance between tool surface and supply lines for the lubrication media must be more than this amount. The consequence is a minimum length of the micro holes of 5 mm to connect the lubrication supply lines with the tool surface and to transport the volatile lubricant into the working zone between tool and metal sheet. To produce micro holes in hardened tool steel with the aforesaid depth and a diameter of around 350 µm, different laser techniques have been developed (see chapter 3). However, one fact links all techniques together: under these conditions, it is currently not possible to manufacture perfect cylindrical micro holes. For reproducible results, drilling conical holes is the only possibility so far. The entrance and exit diameter of the micro hole can be varied arbitrarily inside the system limits of the used laser process. Depending on the position of the laser in relation to the tool, the drilling process results in two different types of conical holes. The first type is a conical micro hole that gradually widens its cross section in the flow direction of the volatile lubricant and the other type is one, which becomes narrower. For the lubrication medium, such shaped micro holes act like a nozzle. Fig. 3, left, shows a hole which becomes narrower along the z-axis and is therefore called a confuser. Contrary to that, the one with opening diameter a diffuser. This definition is generally made for subsonic velocities. In literature [5], the designation for confuser and diffuser is usually switched in fluid mechanics at supersonic velocities. To get a consistent naming here and to avoid a mix-up, the term for the confuser and diffuser is maintained regardless of the flow rate.

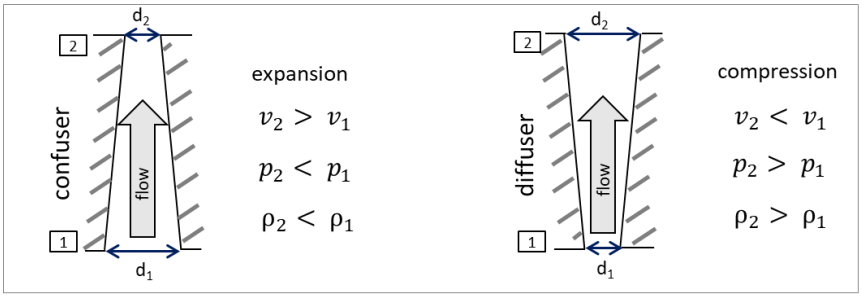


Fig. 3: Comparison of confuser and diffuser at subsonic velocities. Adapted from [6].

For the investigations, compressed $CO_2$ from a gas cylinder with riser pipe was used. At a pressure of around 60 bar and room temperature (20°C), the carbon dioxide is present in equilibrium between liquid and gas phase (see Fig. 4). To examine the influencing factors, which reduces the friction during the deep drawing process, the lubricant fluid flow through the laser-drilled micro holes was investigated using CFD simulations. It is assumed that one effect of friction reduction is the reduction of surface pressure due to the applied lubricant pressure of around 60 bar acting in the interstice between tool and sheet metal. Another effect of friction reduction occurs when using $CO_2$ as volatile medium. It is extracted from the gas cylinder at boiling point. Thus, it is unknown whether $CO_2$ is in solid, liquid or gaseous phase during the forming process and which phase causes a reduction of friction. Furthermore, it is necessary to understand how the geometry of the micro holes influences the pressure and temperature conditions of the volatile lubrication medium before and within the forming zone. Thus, especially the fluid flow of carbon dioxide was simulated. [7]

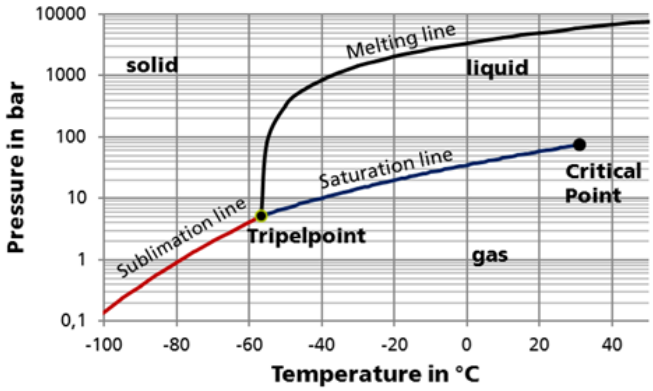


Fig. 4: Phase diagram of $CO_2$ in solid, liquid and gaseous state. [8]

After a first experimental assessment of the fluid flow behaviour, the CFD simulation was implemented in the *COMSOL Multiphysics*® modelling software. For this simulation, the software provides a special tool to solve the equations of the turbulent fluid flow model. For describing the flow of the fluid, the Reynolds-Averaged-Navier-Stokes equations (RANS) were used. For the turbulence modelling the κ-ε-model was included. This model combines an adequate accuracy with a moderate effort. Hence, the fringes of this model were simplified, especially due to an assumed ideal smoothness of the walls so there was no pipe friction implemented. Because of the usage of compressed $CO_2$, it is disadvantageous to work with the ideal gaseous equation. Therefore, the compressibility factor by Peng-Robinson (describes the gaseous- as well as the liquid phase) was implemented. The velocity of the lubricant through the micro holes is high enough to estimate the flow as adiabatic i.e. without heat transfer to the surrounding material. The boundary conditions of the model were set to:

- Constant expansion of the cross-section of the micro hole.
- Mean flow velocity of the lubricant at the inlet.
- Mean pressure at the outlet.
- Free lubricant outflow.
- Adiabatic expansion.

The free outflow is an assumption that is only given at the beginning of the deep drawing process when the press is not completely closed. Additional, free outflow should be avoided to reduce the amount of necessary volatile media. In the further process, a back pressure arises exerting pressure to the exit of the micro holes, thus preventing a free outflow. This back pressure was assumed as the mean pressure at the outlet. To simulate this pressure during the deep drawing process several conditions from 1 bar (atmospheric pressure) up to 21 bar were defined. The inlet flow velocity was estimated by the volume flow and the inlet diameter. Due to the assumptions and simplifications, the exact calculation of pressure level and phase state is not possible. In the CFD-simulations, the two types of micro holes have been implemented. According to the confuser and diffuser geometry, the radii of the inlet and outlet were set to 100 µm and 300 µm respectively. An exemplary sketch for a diffuser-shaped micro hole and the corresponding radii used for the simulation are shown in Fig. 5 a). Because of the provided symmetry of the micro holes, the model was designed as a 2D radius section, to save computing capacity. Afterwards the radius sections can rotate to a 3D model as shown in Fig. 5 b). To simulate the inflow into the micro hole a storage vessel was implemented. The incoming pressure of this vessel was determined to 60 bar. [7]

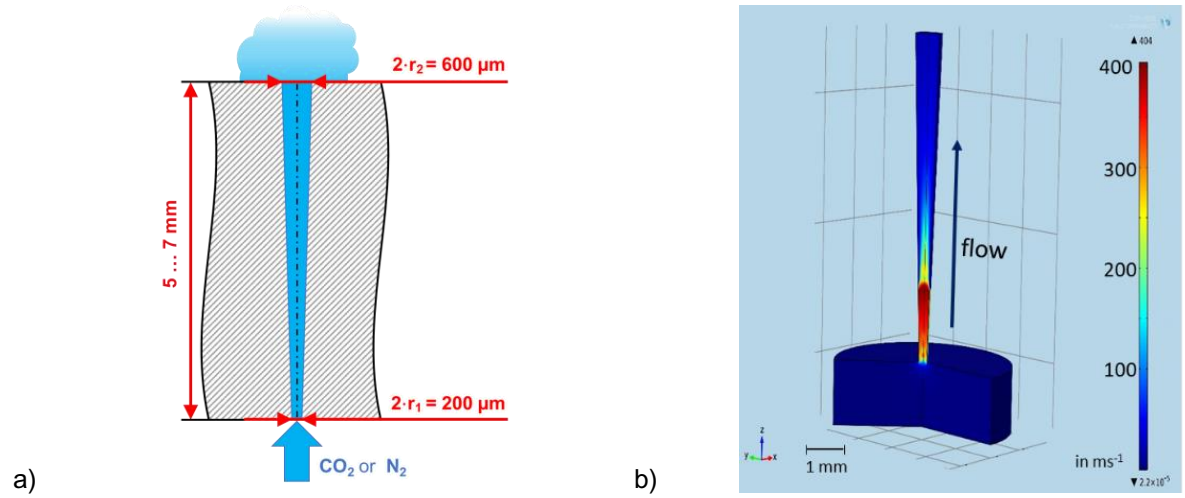


Fig. 5: a) Dimensions of the diffusor-shaped micro hole.
b) 3D fluid flow simulation of the lubricant velocity inside of a diffuser micro hole.

To check the results of the fluid temperature at the outlet, actual temperature measurements were carried out. Therefore, a temperature sensor was placed at the exit of a micro hole. It measured for the diffuser an outlet temperature of around – 20 °C. To include the measurements in the simulations, the models were successively adjusted to the actual temperatures.

To illustrate the differences in terms of velocity, temperature and pressure between the two micro hole types a comparison is shown in Fig. 6. Obviously, the temperature and pressure course inside of the micro hole differs

strongly depending on the nozzle type. Inside the diffuser, a cooling effect down to temperatures around – 50 °C occurs before a compression shock occurs. Therefore, it is plausible that a phase change inside of the diffuser geometry occurs and produces dry ice (see Fig. 4). By contrast, it is most likely impossible to produce dry ice within a confuser. The pressure loss of the convergent micro hole is much lower than within the diffuser. This results in a higher pressure level near to the exit of the confuser. Besides this, the simulation shows a significant increase of the velocity and a decrease of temperature and pressure at the outlet of the confuser. Thus, dry ice formation should occur less around the outlet of the confuser than the diffuser.

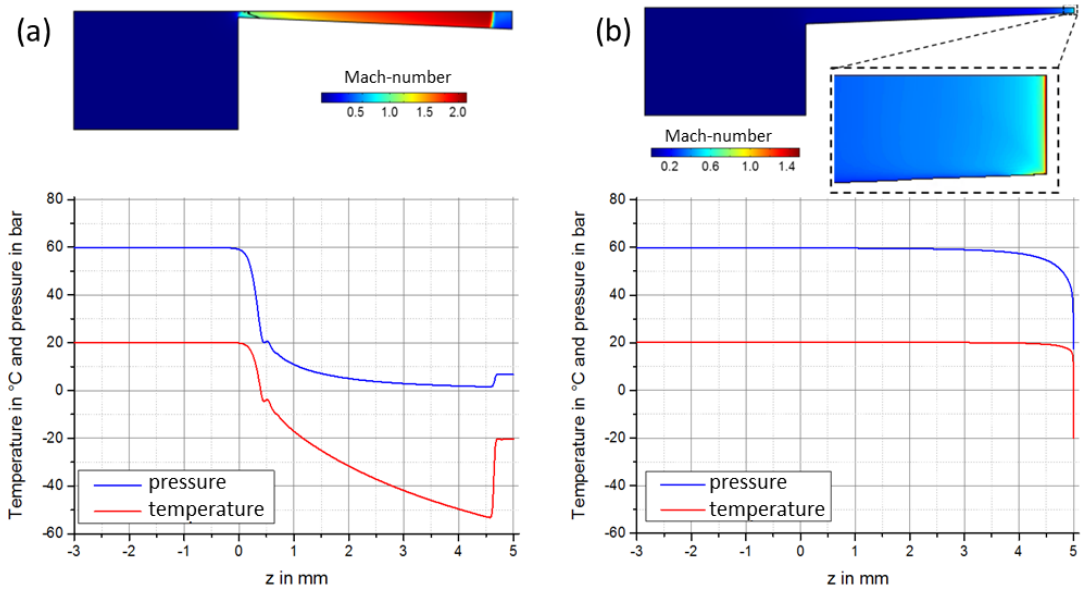


Fig. 6: Comparison of temperature, pressure and velocity of the diffuser (a) and confuser (b) geometry, along the symmetry axis. [7]

The investigations with $N_2$ as lubricant showed a similar behaviour. Though, here is no phase change plausible. By means of these results the first generation of micro holes were designed (see chapter 3). To check the results from the CFD simulations a modified optical strip drawing test was carried out (see chapter 5.1.3). [7]

Besides the CFD simulation of the lubricant flow inside of the micro hole, investigations of the flow between tool and sheet metal were performed. Besides the ideal smooth surfaces, four different surface structures were examined: a structure with circular cells, one with lines and two with asymmetric cells called narrow-deep and wide-deep structures (different depth profile). The models were designed with the CAD software *SolidWorks* and transferred to *COMSOL Multiphysics*® for the CFD simulation. The slide of the sheet metal over the tool with a defined gap of 10 µm, disregarding surface roughness, was investigated. Therefore, a sliding speed of the sheet metal of 100 mm $s^{-1}$ was assumed.

The investigations showed a strong dependence between the sliding speed and the flow velocity of the lubricant. The simulation of the flow behaviour including the surface structures, showed a high turbulent flow inside the interstice. Especially when the line structure and the flow direction are intersecting. This can lead to bad wetting conditions in some areas, comparable to a stall in aerodynamic. In the actual forming process, this would cause a direct metal-metal contact without any lubrication. The fluid flow using the different types of cups showed a similar behaviour. The line-structure running in flow direction (like a star with the micro hole as its centre) showed a significant decrease of lubricant pressure between tool and metal sheet. This is caused by the line structure as it allows the lubricant to escape. Hence, the lubricant flows through the structure directly out of the interstice, without lubricating the process. By structuring the surface, it was intended to create a kind of lubricant reservoir, but the investigations showed, that the lubrication medium used in this research is not comparable to conventional mineral oil-based lubricants. To verify these results under more realistic conditions, strip drawing tests were carried out (see chapter 5.1.4). [4]

## 3 Laser-drilling of deep micro holes with ultrashort pulsed laser radiation

### 3.1 Limits for drilling of deep micro holes

As described above, conically shaped micro holes with a depth of several millimetres are required in the forming tools. Laser drilling with ultrashort laser pulses promises drilling of high-quality micro holes that meet the requirements. However, laser-drilling of deep micro holes into hardened tool steel is still a major challenge. Decreasing quality with increasing depth of the micro holes was observed and reported in numerous publications, e.g. in [9]. One of the major reasons for reduced quality during laser processing with ultrashort laser pulses is the so-called heat accumulation. In addition, the limited pulse energy evidently limits the maximum drilling depth: With increasing hole depth the total wall surface area of the micro hole increases. This means that the average laser fluence (i.e. the laser pulse energy divided by the wall surface area) decreases. If the average fluence reaches the ablation threshold fluence, only very slow and localized drilling can occur. This limit is called "quality depth limit" in the following. Heat accumulation and the quality depth limit were investigated for the required geometry of the micro holes.

The prototype kW-class ps-laser of the IFSW was used for the experiments [10]. The passive disk laser amplifier allows for very high pulse energies, which are necessary for the drilling of very deep micro holes. A helical drilling optic (GL-Trepan) was used to move the focused laser beam along a circle path over the surface of the sample and to precisely adjust the diameter of the circle. Furthermore, GL-Trepan allows adjusting the inclination angle of the beam relative to the surface, which is useful for longitudinal shaping of the holes. The properties of the laser, the helical drilling optics, and the focusing optics are summarised in Tab. 1.

Tab. 1: Properties of the IFSW kW-class-ps laser system and the helical drilling optics.

| IFSW kW-ps laser [10] | | |
|---|---|---|
| Pulse duration | $\tau$ | 8 ps |
| Wavelength | $\lambda$ | 1030 nm |
| Average power | $P$ | ≤ 650 W |
| Max. pulse energy | $E_p$ | ≤ 2.2 mJ |
| Repetition rate | $f_{rep}$ | ≤ 300 kHz |
| Beam Quality | $M^2$ | < 1.3 |
| Raw beam diameter | $D_r$ | 5.2 mm |
| Polarization | | Linear |
| **Helical drilling optics (GL-Trepan, GFH GmbH)** | | |
| Rotation speed | | 0-30'000 rpm |
| Hole diameters | | 0-1500 µm |
| Inclination angle | | 0° - 4° |
| **Focusing and ablation threshold** | | |
| Focal length | $f$ | 400 mm |
| Focus diameter | $w_0$ | 140 µm |
| Polarization | | Circular |
| Focus position | | On the surface |
| Max. peak fluence | $\Phi_0$ | 32 J/cm$^2$ |
| Ablation threshold (steel, 8 ps, 1030 nm) | $\Phi_{th}$ | 0.1 J/cm$^2$ |

#### 3.1.1 Heat accumulation limit

Heat accumulation was identified as one of the major quality-reducing effects for deep-hole drilling [11], [12]. It is the main cause of burr formation at the laser impact side of the micro hole and the formation of a heat-affected zone during laser drilling with ps-lasers. Only a part of the energy absorbed by each individual laser pulse is used for material ablation. The remainder of the absorbed energy $\eta_{Heat}$ remains as heat in the non-

removed material and, if it cannot be dissipated quickly enough by heat conduction, results in a constant increase in the temperature of the workpiece during continuous laser operation.

In the case of pulsed energy input and two-dimensional heat conduction, as can be assumed for a micro hole, the distribution of the temperature increase in the x-and y-direction can be calculated as a function of time by the following equation. [11]

$$\Delta T_{Sum,2D}(x,y,t) = \frac{\eta_{abs} \cdot \eta_{Heat} \cdot E_{pulse}/s_{hole}}{\rho \cdot c_p \cdot 4\pi \cdot \kappa} \sum_{N=1}^{N_p} \frac{\Theta\left(t - \frac{N-1}{f_L}\right)}{\sqrt{\left(t - \frac{N-1}{f_L}\right)^{nD}}} exp\left(-\frac{x^2+y^2}{\left(t - \frac{N-1}{f_L}\right) \cdot 4\kappa}\right) \cdot \quad (1)$$

Here $s_{hole}$ is the depth of the micro hole, $E_{pulse}$ is the pulse energy, $\eta_{abs}$ is the absorptance, and $\eta_{Heat}$ is the part of the energy that is coupled into the micro hole that remains as heat in the material. The absorbed energy is assumed to be homogeneously distributed in the micro hole, $\rho$, $c_p$ and $\kappa$ are the material parameters density, specific thermal capacity and thermal conductivity. $\Theta$ is the Heaviside function and $N_P$ is the number of laser pulses at the repetition rate of $f_L$. The variables $x$ and $y$ are spatial coordinates.

The temperature increase calculated at the time immediately before the next pulse and at the coordinate origin is shown in Fig. 7 for the repetition rates of 300 kHz (a) and 60 kHz (b). A micro hole depth of 1 mm and $\eta_{abs} \cdot \eta_{Heat}$ = 13% was assumed. At the pulse repetition rate of 300 kHz, the temperature exceeds the melting temperature of the steel (dotted line) by 0.5 ms, i.e. by about 150 pulses, whereas at 60 kHz the temperature does not exceed 600 K. The use of a lower pulse frequency is therefore a fundamental condition - especially with the necessary high pulse energies - for reducing or avoiding the accumulation of heat and the resulting reduction in micro hole quality due to melt formation. Experiments with low pulse energies confirmed the calculations of this model [11].

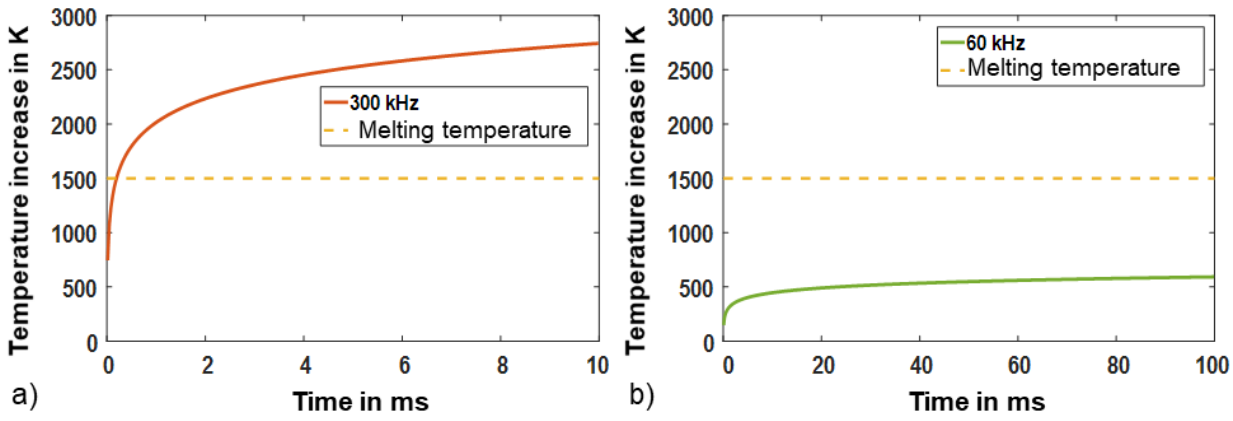


Fig. 7: Calculated temperature increase by heat accumulation as a function of process time for a drilling depth of 1 mm at pulse energy of 1,3 mJ at 300 kHz (a) and 60 kHz (b). Calculated temperature increase by heat accumulation as a function of process time for a drilling depth of 1 mm at a pulse energy of 1,3 mJ at 300 kHz (a) and 60 kHz (b). Adapted from [13].

### 3.1.1.1 Validation of heat accumulation for higher pulse energies

The results of drilling experiments with pulse energies of up to 2.2 mJ at a reduced repetition rate are presented below to validate the previously described model of heat accumulation for higher pulse energies. Drilling was performed with repetition rates between 15 kHz to 100 kHz with $10^6$ pulses each. For these experiments, non-hardened samples of tool steel 1.2379 with a thickness of 5 mm were used.

The optically measurable occurrence of phase transitions in the material indicates a heat-affected zone, which was defined as an indicator for a reduced quality. These phase transformations include the formation of melt (T ≈ 1500 K) as well as a solid phase transformation (T ≈ 600 K). While the formation of melt is visible on the sample surface, the solid state phase transformations were analysed by polishing and etching of the cross-sections with Nital 5% for 40 seconds. Cross-sections are shown in Figure 5. The repetition rate increases from left to right. Due to the different amplification of the laser system at different repetition rates, the pulse energy varies slightly.

At low repetition rates of 15 kHz and 30 kHz, the samples were not drilled through completely with $10^6$ laser pulses. Fully drilled micro holes could only be produced at 60 kHz and 100 kHz. In the case of micro holes produced at a repetition rate of ≤ 60 kHz, only a small heat-affected zone can be detected. The heat-affected zone can be identified by the orange shading, which becomes visible after etching. At the repetition rate of 100 kHz, a heat-affected zone of approximately 300 µm has formed around the micro hole (see Fig. 8 d).

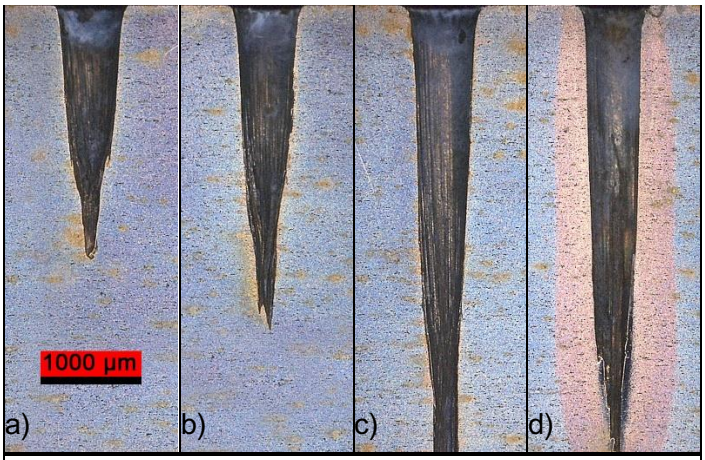


| 15 kHz | 30 kHz | 60 kHz | 100 kHz |
|---|---|---|---|
| 2.1 mJ | 1.5 mJ | 2.0 mJ | 2.1 mJ |
| Approximately $10^6$ pulses | | | |

Fig. 8: Cross-sections of micro holes at different repetition rates. For a repetition rate of 100 kHz, a heat-affected zone of approximately 300 µm was formed around the micro hole due to heat accumulation. Adapted from [13].

### 3.1.1.2 Effects of heat accumulation in hardened tool steel

The effects in hardened tool steel when drilling with very high average laser power were investigated [13]. The same setup as described previously was used, featuring a pulse energy of 2.2 mJ and a repetition rate of 300 kHz, which resulted in an average laser power of 660 W. More than 200 micro holes were drilled into samples of hardened tool steel.

Subsequently, however, more than 80 % of the samples showed cracks after 72 h. Some of the cracked samples were microscopically examined to determine the causes of crack propagation. Fig. 9 shows a typical crack pattern. Polishing and etching the samples with Nital 3 % for 35 s reveals a heat-affected zone of approximately 0.8 mm in the vicinity of the micro hole.

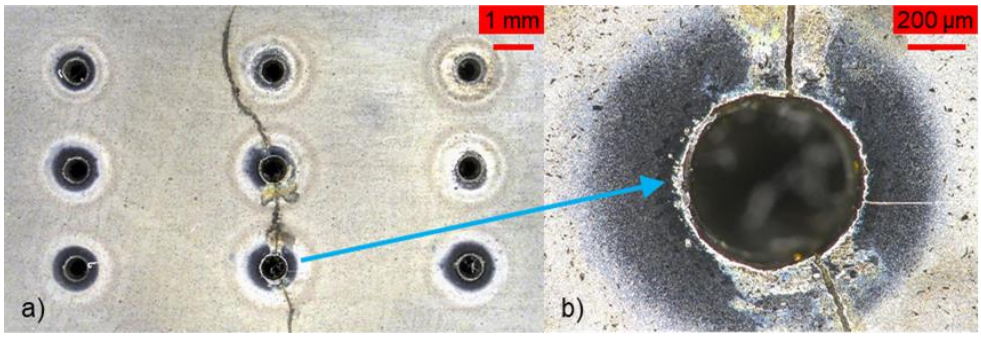


Fig. 9: a) Example of a cracked sample; b) Magnification of (a) shows the microstructure of the sample: "primary large carbides" (PLC) can be identified by dark spots. Adapted from [13].

The crack originated from the micro holes. Fig. 9 b) shows the enlarged microstructure in the vicinity around a micro hole. Although many dark areas of irregular shape and size between 20 µm and 50 µm are visible that indicate "primary large carbides" (PLC), these could not have been the only reason for crack formation. However, according to [13], these can serve as crack nucleation sites, which may have been responsible for cracking in combination with the low fracture strength of the tool steel (20 MPa $\cdot \sqrt{m}$). This assumption is supported by the fact that no failure occurred in unhardened samples during laser processing with the same process parameters, although these unhardened samples have the same chemical composition and distribution of carbide.

### 3.1.2 Depth limit

As the drilling depth increases, the wall surface area within the micro hole also increases. This means that the average incident fluence, i.e. the pulse energy divided by the micro hole wall surface area, decreases. As soon as the mean fluence falls to the materials ablation threshold fluence, a significantly decelerated and discontinuous drilling progress occurs. This point is also known as the 'Quality Depth Limit' or 'Phase 1' [12], and describes the boundary to which fast, efficient drilling is possible.

This limit can be observed, when the drilling depth is plotted as a function of the number of laser pulses. In the following example, the same setup as described in section 3.1 was used to drill micro holes with five different repetition rates, ranging from 30 kHz to 300 kHz at a constant pulse energy of 2.2 mJ [14]. The results are shown in Fig. 11.

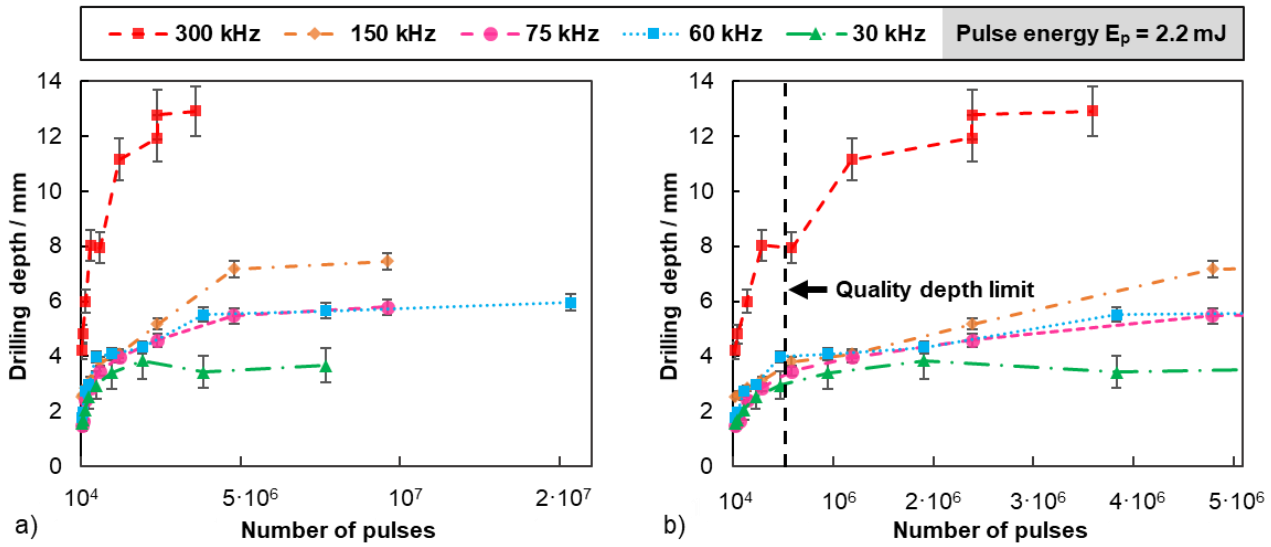


Fig. 10: a) Micro hole depth as a function of the number of pulses for the pulse energy of 2.2 mJ for different repetition rates.
b) Magnification of a) shows the drilling progress for a smaller number of pulses to highlight the 'quality depth limit'. Adapted from [14].

The significantly accelerated drilling progress for a repetition rate of 300 kHz clearly indicates a melt-assisted drilling process due to heat accumulation when compared to lower repetition rates. For repetition rates of 150 kHz and below the drilling progress is quite similar. Up to about $5 \cdot 10^5$ pulses, the drilling progresses very fast to a depth of about 4 mm. As the depth further increases, the progress becomes slow and irregular. The faster drilling progress after $2 \cdot 10^6$ pulses for the repetition rates > 30 kHz suggests, that after a very large number of pulses, heat accumulation gains influence. It can be assumed that the 'quality depth limit' for pulse energies of 2.2 mJ is reached at about 4 mm (marked by the dashed vertical line in Fig. 10 b).

For an ablation-dominant percussion drilling process, Förster et. al [15] have developed a simplified analytical model that allows for the prediction of the achievable drilling depths (previously mentioned as 'Quality Depth Limit') or aspect ratio for a given spot diameter and pulse energy. This model is based on the following boundary conditions. Effects such as nonlinear absorption and heat accumulation are to be avoided. The formation of a conical micro hole geometry is assumed, as described in numerous publications [16]–[19]. Furthermore, a homogeneous distribution of fluence inside the conical micro hole is assumed.

On the basis of the above mentioned assumptions, the basic equation for the achievable drilling depth $z_{depth}$ was derived, which depends only on the incident fluence $\phi_0$, the beam radius $w_0$ and the material ablation threshold $\phi_{th}$, shown in equation (2) [15].

$$\frac{z_{depth}}{w_0} = \sqrt{\frac{{\phi_0}^2 - {\phi_{th}}^2 \cdot \ln^2\left(\frac{\phi_0}{\phi_{th}}\right)}{2 \cdot {\phi_{th}}^2 \cdot \ln\left(\frac{\phi_0}{\phi_{th}}\right)}} \,. \tag{2}$$

The validity of the prediction expressed by this analytical model was confirmed by corresponding percussion drilling experiments. Three different focal radii of 45 µm, 23 µm, and 13 µm where used, which correspond to a maximum peak fluence of 5 J/cm², 19.3 J/cm² and 60.3 J/cm². The focal plane was set on the surface of the

drilled samples. An ultrafast solid state laser (Duetto, Lumentum) with a repetition rate of 5 kHz was used to prevent quality deterioration due to heat accumulation and excessive melt. The laser wavelength was 1064 nm and the maximum pulse energy was 160 µJ. The pulse duration was 10 ps and the laser beam was circularly polarized.

Fig. 11 depicts the ratio of drilling depth over the beam radius as function of the incident fluence. The experimental results (data points with error bars) are plotted together with the calculated ratio according to the analytical model (black line surrounded by gray hatch, representing the model with a variance of the ablation threshold of 0.09 ± 0.02 J/cm²). Example cross-sections of corresponding micro holes are shown at the top, indicated with arrows. Adapted from [15].

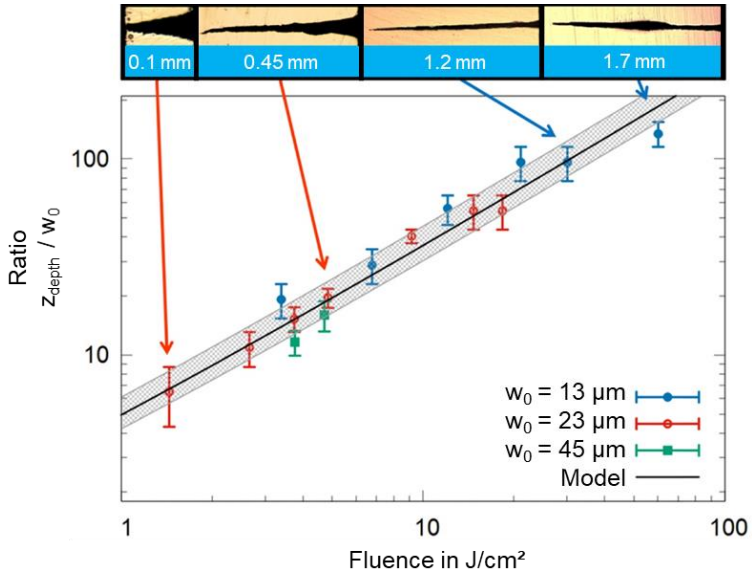


Fig. 11: Experimental results (data points with error bars) and ratio of drilling depth over beam radius calculated from the analytical model (black line surrounded by gray hatch, representing model with a variance of the ablation threshold of 0.09 ± 0.02 J/cm²). Example cross-sections of corresponding micro holes are shown at the top, indicated with arrows. Adapted from [15].

The proposed model was also applied to determine the requirements for unconventionally deep micro holes, as required for the application in dry metal forming using volatile lubricants. For proof of concept a sample thickness of 10 mm was chosen to be drilled through. The thin-disk laser amplifier, previously described in section 3.1, was used for this experiment. However, the pulse energy was set to 3 mJ. In order to avoid heat accumulation effects, the repetition rate was set to 30 kHz, which resulted in an average laser power of 90 W.

According to equation (1), a focal radius of approximately 59 µm or less is necessary to reach the drilling depth of 10 mm with a given pulse energy of 3 mJ. Due to the elliptical beam profile of the laser beam, the resulting beam radii in the focal position were $w_{0,x}$ = 53 µm (1/e² major semi-axis) by $w_{0,y}$ = 38 µm (1/e² minor semi-axis). A cross-section of the resulting micro hole is shown in Fig. 12. In addition, the polished cross-section was etched with the Adler etchant (solution of water, ammonium chlorocuprate, hydrochloric acid and ferric chloride) to highlight a possible structural change that would indicate a heat-affected zone. As can be seen, no thermal damage (structural change) occurred. The number of pulses required to drill this micro hole was approximately $1.22 \cdot 10^7$, resulting in a drilling time of 6 minutes and 48 seconds

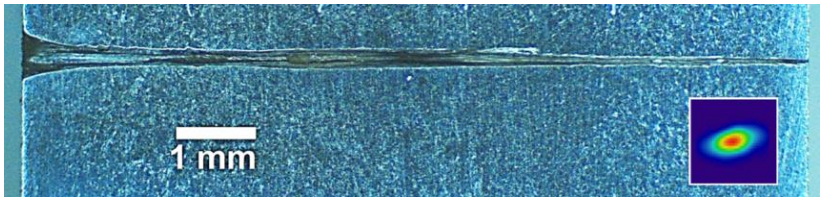


Fig. 12: Through hole in 10 mm stainless steel (1.4301), etched (Adler); entrance diameter approx. 410 µm (left side), outlet diameter approx. 52 µm (right side); the beam profile of the used high energy ps laser is displayed in the inset on the right. The number of pulses required to drill this micro hole was approximately 1.22·107, resulting in a drilling time of 6 minutes and 48 seconds. Adapted from [15].

## 3.2 Longitudinal shaping of micro holes

In the previous chapter the limits of drilling with ultrashort pulses were discussed. In the following, this knowledge served as a foundation for a more precise design of the micro holes. In particular, the longitudinal shaping of micro holes for a percussion drilling process was investigated.

### 3.2.1 Micro hole radius on the side of the laser impact

The radius of the micro hole on the side of the laser impact is determined by the ablation radius. The ablation radius is determined by the ablation threshold $\phi_{th}$, i.e. where the local fluence $\phi$ in the Gaussian shaped beam profile is equal to the ablation threshold of the material. According to [20] the ablation radius can be calculated analytically and is given by

$$r_{abl}(z, E_p) = r_{beam}(z) \cdot \sqrt{\frac{1}{2} ln \left( \frac{2 \cdot E_p}{\pi \cdot r_{beam}(z)^2 \cdot \phi_{th}} \right)} . \tag{3}$$

The ablation radius is thereby dependent on two main parameters: the pulse energy $E_p$ and the beam radius $r_{beam}(z)$, which in turn is a function of the position along the laser beam propagation in z direction and is given by

$$r_{beam}(z) = w_0 \cdot \sqrt{1 + z^2 \cdot \left( \frac{M^2 \cdot \lambda}{\pi \cdot w_0^2} \right)^2} , \tag{4}$$

where $w_0$ is the radius of the beam in the focus, $M^2$ the beam quality and $\lambda$ the wavelength of the laser beam.

Fig. 13 shows the beam radius $r_{beam}(z)$ along the propagation direction $z$ (the ordinate) for a focal length of 600 mm and a raw beam diameter on the focussing lens of 10 mm as a dotted red line. In addition, the ablation radius $r_{abl}(z)$ is plotted for the pulse energy of $E_p$ = 0.5 mJ (blue line) and for $E_p$ = 5 mJ (green line). The ablation radii near the focal point, at z = 0, are similar for both pulse energies. However, this changes for increasing $z$. In the case of a pulse energy of 0.5 mJ, ablation is only possible for z < 45 mm. Furthermore, it is seen, that the pulse energy of 0.5 mJ is not sufficient to produce an ablation radius of 300 µm (marked with the vertical dash-dotted black line). In comparison, an ablation radius of about 400 µm is achieved at z = 45 mm with a pulse energy of 5 mJ, whereas the ablation radius of 300 µm is achieved at z ≈ 27 mm.

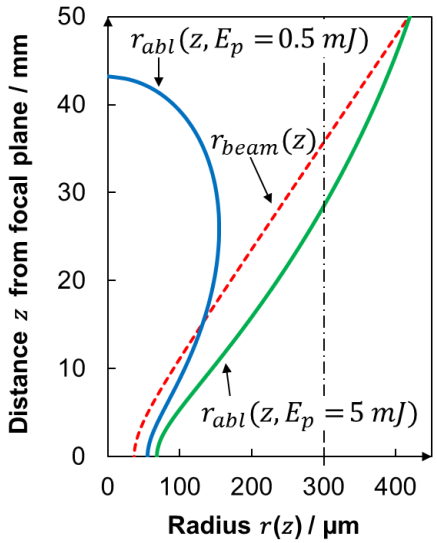


Fig. 13: shows the beam radius $r_{beam}(z)$ along the propagation direction $z$ (ordinate) as a dashed red line. In addition the ablation radius $r_{abl}(z)$ is plotted for the pulse energy of $E_p$ = 0.5 mJ (blue line) and for $E_p$ = 5 mJ (green line). Adapted from [20].

The ablation radius for any position in z-direction of the sample relative to the focus position can be determined using the analytical model shown in this chapter with the given pulse energy and ablation threshold.

### 3.2.2 Required laser pulse energy

Based on the model presented by Förster et. al [15], the pulse energy $E_p$ for a desired ablation radius $r_{abl}$ and a given drilling depth $z_{depth}$ can be written as

$$E_p = \phi_{th} \cdot \pi \cdot r_{abl} \cdot \sqrt{r_{abl}^2 + z_{depth}^2} \quad . \tag{5}$$

In order to create a conical micro hole with a required ablation radius of $r_2$ = 300 µm and the required drilling depth of 5 mm, the necessary pulse energy amounts to approximately 4.4 mJ. For this example, a threshold fluence for steel of $\phi_{th}$ = 0.09 J/cm², at a wavelength of 800 nm and a pulse duration of 1 ps, was chosen.

### 3.2.3 Experimental setup and results

The Spectra Physics Spitfire Ti:Sapphire laser financed by the DFG was used for the experiments. The specifications of the laser beam source are listed in Tab. 2. The low repetition rate of 1 kHz ensured that heat accumulation was avoided as described in chapter 3.1.1. The experimental setup is sketched in Fig. 14. The linearly polarized raw laser beam was circularly polarized passing through a λ/4 wave plate, and focused with a quartz focusing lens with a focal length of $f$ = 600 mm onto the samples, which were mounted on a xyz-translation stages. The two axes x and y were used for repositioning the sample for the individual micro holes. The z-axis was used to set the distance of the sample in the beam propagation direction relative to the focal plane (represented by dashed gray rectangles) allowing to set the spot size on the sample surface. With the raw beam diameter of $D_r$ = 10 mm, the calculated focus radius was approximately $r_{beam}(z = 0) = w_0$ = 37 µm. Due to the good availability, stainless steel (1.4301) was used as sample material.

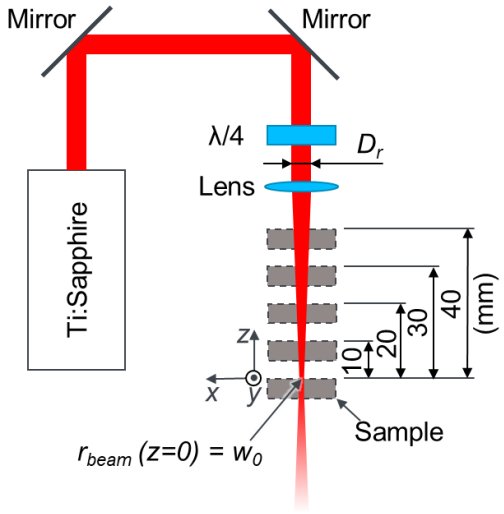


Tab. 2: Process parameters used for the experiments.

| Spectra Physics Spitfire H | | |
|---|---|---|
| Pulse duration | $\tau_p$ | 100 fs; 1 ps |
| Wavelength | $\lambda$ | 800 nm |
| Average power | $P$ | ≤ 7 W |
| Max. pulse energy | $E_p$ | ≤ 7 mJ |
| Repetition rate | $f_{rep}$ | 1 kHz |
| Beam Quality | $M^2$ | ≤ 1.2 |
| Raw beam diameter | $D_r$ | 10 mm |
| Polarization | | Linear |
| **Focusing and ablation threshold** | | |
| Focal length | $f$ | 600 mm |
| Focal radius | $w_0$ | 37 µm |
| Polarization | | Circular |
| Focus position | | Variable |
| Max. peak fluence | $\Phi_0$ | 236 J/cm² |
| Ablation threshold (steel, 1 ps, 800 nm) | $\Phi_{th}$ | 0.09 J/cm² |

Fig. 14: Experimental setup (left). The linearly polarized raw laser beam with a beam diameter of $D_r$ = 10 mm was circularly polarized with a λ/4 wave plate, and focused with a quartz focusing lens with a focal length of $f$ = 600 mm onto the samples, which were mounted on a xyz-translation stages. The z-axis was used to set the distance of the sample in the beam propagation direction relative to the focal plane (represented by dashed grey rectangles) allowing to set the spot size on the sample surface. [20]

Five micro holes were drilled at increasing z-distances for both 1 ps and 100 fs pulse durations as shown in Fig. 15. The z-positions were z = 0 mm, 10 mm, 20 mm, 30 mm and 40 mm. The experimental results are shown in Fig. 15. For both pulse durations cross-sections are shown on the top (a and b) and the measured ablation radii for the corresponding z-positions are plotted in the graphs below (c and d), which are indicated as blue rhombs. The data points are connected with a dotted line to guide the eye. The calculated model of the ablation radius for a given pulse energy of 5 mJ according to eq. (3) are plotted as solid green line. For both cases, the fluence threshold was set to 0.05 J/cm² in order to fit to the measured values.

For the pulse duration of 1 ps the measured ablation radii are very close to the model. For z ≤ 10 mm, only a small increase of the radius is noticeable. However, laser pulses with short pulse duration and high pulse energy can cause an air breakdown, particularly in the vicinity of the focus, if an undisturbed irradiance of more than $10^{14}$ W/cm² is achieved [18], [21]. The ionization of the air causes a change of the refractive index resulting in defocusing of the incident laser beam. This results in an increased spot size on the sample surface and therefore a change of the ablation radius compared to the calculated model. This effect is particularly pronounced when the pulse duration is further reduced to the femtosecond range, as shown for 100 fs on the right hand side of Fig. 15. In both graphs, the undisturbed irradiance at the position of the sample surface is given on the right y-axis. As can be seen very clearly in Fig. 15 d), with increasing irradiance, the deviation towards larger ablation radii becomes more prominent.

The quality of the micro hole can be significantly improved by avoiding an air breakdown, as can be seen very clearly by comparing the two series of cross sections.

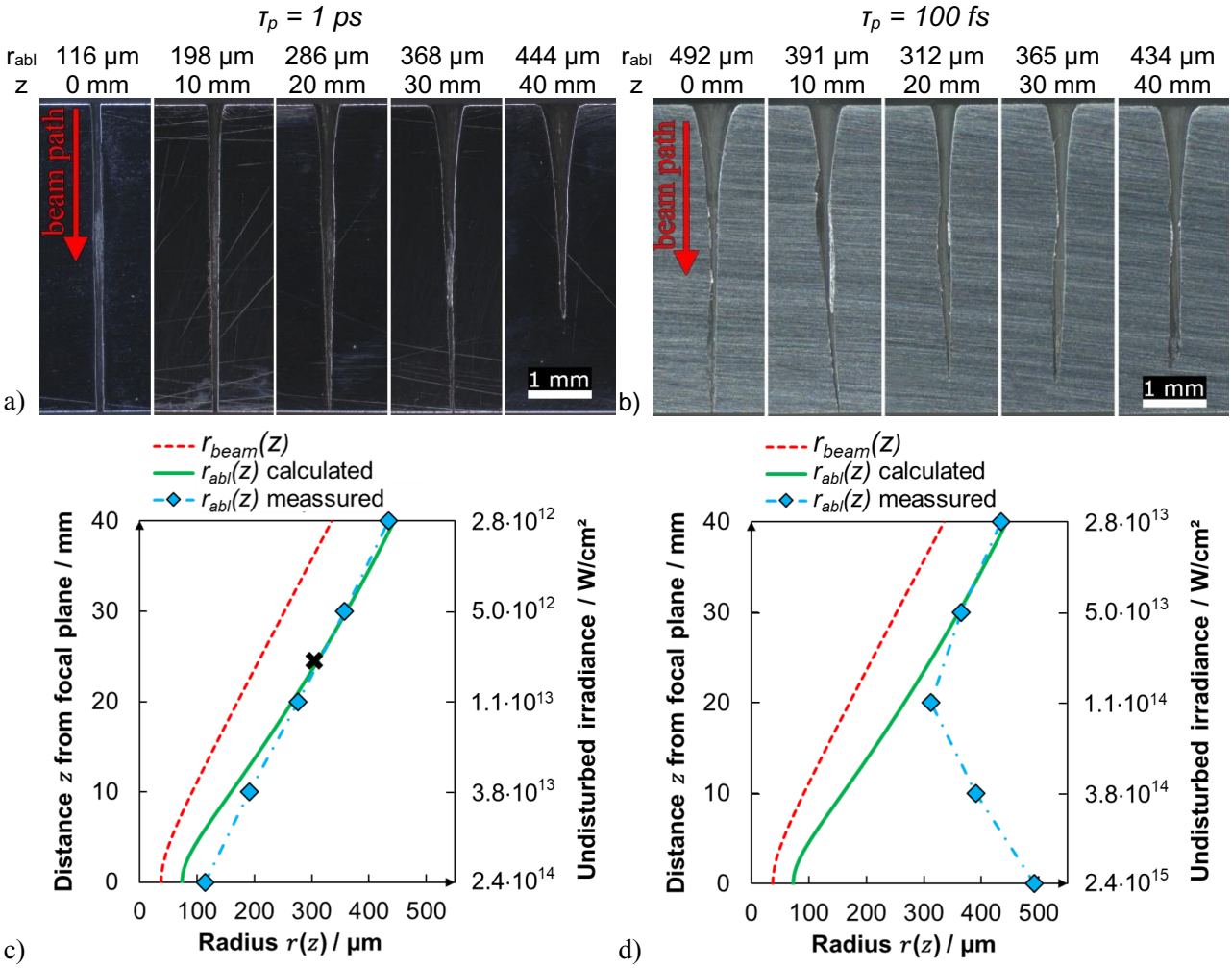


Fig. 15: a) and b) cross-sections for increasing distances in z with the corresponding measured ablation radii ($r_{abl}$) for both pulse durations $\tau_p$ = 1 ps and $\tau_p$ = 100 fs at a pulse energy of 5 mJ; c) and d) calculated (green line and measured (blue rhombs) ablation radii ($r_{abl}$) plotted for increasing z. The data points are connected with a dotted line to guide the eye. In addition, the beam radius $r_{beam}(z)$ is drawn as a dashed red line. For this example, the fluence threshold was set to 0.05 J/cm² to fit the measured values. Adapted from [20].

### 3.3 Approaches to improve the quality of micro holes

In this chapter, the different drilling strategies and the achievable quality of the respective drilled micro holes are compared.

#### 3.3.1 Longitudinal beam displacement

With the knowledge gained from chapter 3.2, it was possible to adapt a drilling strategy whereby the relative longitudinal displacement of the laser beam to the sample surface is used to produce a micro hole with the

required properties. In order to meet the required outlet radius in the forming tool of $r_2 = 300$ µm with the ablation radius, a distance of approximately z = 25 mm between the sample surface and the focus position was necessary (marked with a cross in Fig. 15 c) at a pulse duration of 1 ps and a pulse energy of 5 mJ.

For this example, the sample material was hardened tool steel (1.2379). The two steels 1.4301 and 1.2379 showed very similar results with the same drilling parameters. Fig. 16 shows a cross-section of such a micro hole. The sample was etched with an Adler solution for 30 seconds. The effect of heat accumulation was successfully avoided as no heat-affected zone is apparent. Apart from a small transverse bulge in the upper half, the form of the micro hole is approximately diffusor-shaped, and therefore very close to the ideal shape as described in chapter 2. In addition, cross-sections of the outlet (top) and inlet (bottom) of the volatile lubricants are shown on the right-hand side. Equivalent cross-sectional circles are marked with dotted lines where the radius was approximately $r_2 = 300$ µm and $r_1 = 50$ µm, respectively. The shape of the circumference of the hole on the important outlet side is very close to the required circle. On the inlet side, the shape of the circumference is rather rectangular than circular. However, the shape on the inlet side is not affecting the property of the volatile lubricant at the outlet side. About $2.1 \cdot 10^5$ pulses were necessary for the production of this micro hole.

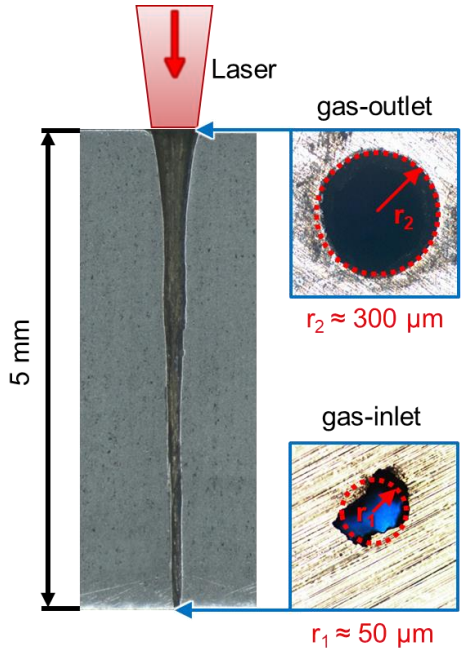


Fig. 16: Cross-section of a micro hole in hardened tool steel (1.2379), etched with an Adler solution for 30 seconds (left). In addition, the gas-outlet (top) and gas-inlet (bottom) cross-sections are shown on the right-hand side. The dotted circles represent equivalent cross-sectional areas where the radius was approximately $r_2 = 300$ µm and $r_1 = 50$ µm, respectively. [20]

### 3.3.2 Transverse beam deflection

Additional control of the micro hole shape can be achieved by transversal beam movement. The following example briefly describes the movement of the laser beam in the plane perpendicular to the beam propagation. This requires optical components that allow continuous beam deflection, such as scanner optics.

The IFSW kW-class-ps laser described in section 3.1 was used for this experiment in combination with a galvanometer-scanner and a telecentric f-theta lens. The laser was operated at the pulse energy of 2.7 mJ at the repetition rate of 30 kHz, resulting in an average power of approximately 80 W. The experimental setup is sketched in Fig. 17 a). The linearly polarized raw laser beam was circularly polarized with a λ/4 wave plate before entering the galvanometer-scanner. In combination with a telecentric lens, the laser beam could be deflected in x and y direction while remaining parallel to the original beam propagation direction. In the example shown the laser beam is moved along a spiral on the sample surface. For this experiment, stainless steel (1.4301) with a thickness of 6 mm was used.

Fig. 17 b) shows a cross-section of a micro hole produced with this setup. The conical shape of the micro hole is very smooth and therefore ideally suited for the transport of the volatile lubricants. In addition, the gas-outlet (top) and gas-inlet (bottom) cross-sections are shown on the right-hand side. Equivalent cross-sectional areas

are marked with dotted circles where the radius was approximately $r_2 = 300$ µm and $r_1 = 100$ µm, respectively. The sizes of both gas-in- and outlet meet the requirements very precisely. About $1.35 \cdot 10^6$ pulses were necessary for the production of this micro hole.

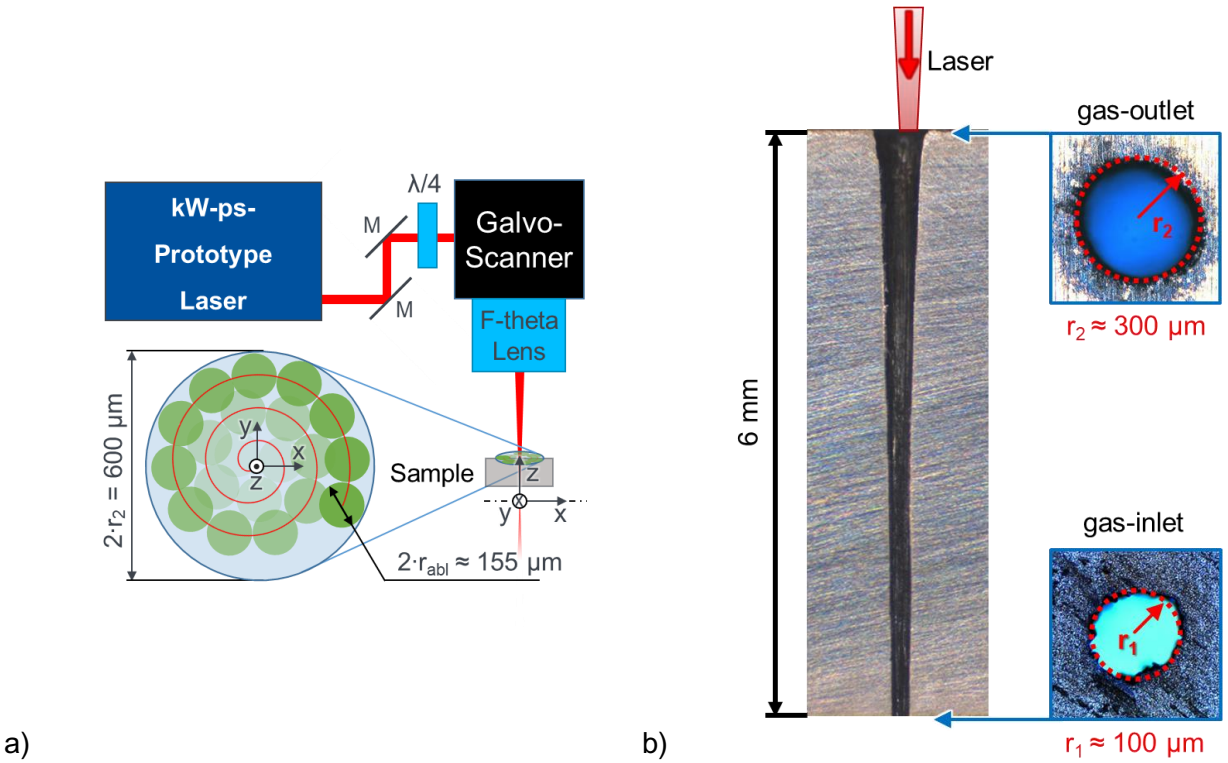


Fig. 17: a) Experimental setup (left). Before entering the galvanometer-scanner, the linearly polarized raw laser beam was circularly polarized with a λ/4 wave plate. The galvanometer-scanner in combination with a telecentric lens allows for a parallel shift of the laser beam in x and y directions. This allows the laser beam to be moved along a spiral path on the sample surface, as shown in this example.

b) Cross-section of a micro hole in stainless steel (1.4301), produced with the setup shown in a). In addition, the outlet (top) and inlet (bottom) cross-sections are shown on the right-hand side. The dotted circles represent equivalent cross-sectional areas where the radius was approximately $r_2 = 300$ µm and $r_1 = 100$ µm, respectively.

### 3.4 Laser drilling of the forming tools

As described in chapter 3.2, the distance from the position of focus to the surface of the workpiece can be used to shape a micro hole. The exact knowledge of this position in relation to the workpiece is therefore crucial for the reproducibility of a larger number of micro holes. This parameter is easy to control on flat surfaces. However, if the micro holes are to be drilled at a certain angle to the normal vector of a surface or to the surface of a radius, the effort involved in maintaining the mentioned distance increases. Since the laser beam is a contact-free tool, it is also more difficult to determine the distance.

In the course of this project, a number of tools with different shapes and sized were laser-drilled. These include jaws used for the flat strip drawing tests (see chapter 5.1), the radius tools used for the stretch-bending tests (see chapter 5.3) and finally the forming tools used in the feasibility studies to produce rectangular cups as described in chapter 7.

The laser-drilling of the forming tool regarding the production of rectangular cups includes all of the above mentioned difficulties, since it features angled micro holes on the main surface of the tool as well as micro holes on the radius. The three-dimensional positioning of the forming tool blank is therefore critical. Most laser micromachining systems are equipped with linear translation stages, which enable the positioning of usually smaller workpieces in relation to the stationary focus of the laser beam. Drilling at a certain angle therefore requires additional fixtures to adjust the workpiece rotation.

A different approach will be taken for the upcoming improved forming tool to be used for the endurance investigations described in chapter 8.2. In this example, the upper part of the forming tool remains in a stationary position and the laser beam is moved with the help of three linear and two rotational axes. Such a setup is

shown Fig. 18, where a galvanometer-scanning head from Scanlab in combination with a telecentric f-theta lens can be angled in any orientation to the tool blank.

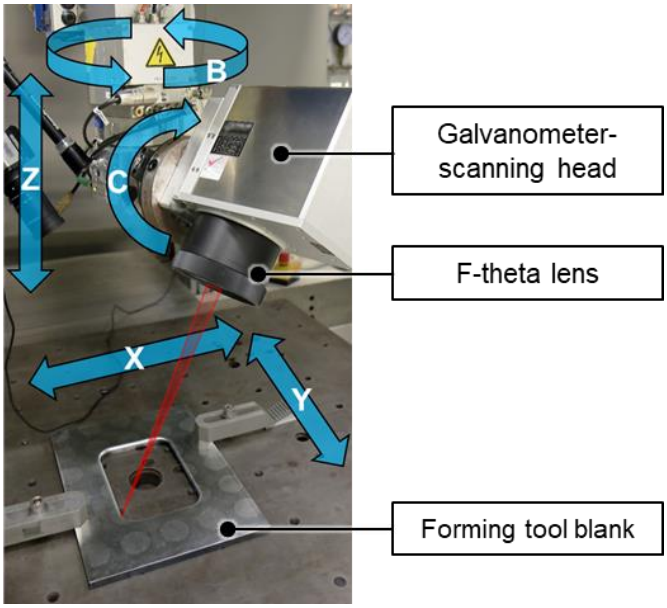


Fig. 18: New setup for laser-drilling of the improved version of the forming tool blanks for the upcoming endurance investigations. The galvanometer-scanning head in combination with a telecentric f-theta lens can be angled in any orientation to the tool blank.

## 4 Pressure Chamber Tests

As shown in the chapter of the CFD simulations the two micro hole geometries cause a completely different flow behaviour and in case of $CO_2$ also the phase state. In dependence of temperature and pressure during the process, the physical state of the $CO_2$ changes (Fig. 21). As a consequence the wetting of the tool as well as the friction in the process is significantly affected. As shown before in the chapter on CFD simulations, the conical drilled micro holes act like a nozzle, hence the fluid flow behaviour depends strongly on the used type of micro hole. To investigate these effects a pressure chamber was constructed. Wetting and de-wetting of different surfaces was examined. In the process window Nitrogen stays always gaseous, so it was not possible to examine the wetting behaviour of this lubrication medium. Hence, the tests were limited to carbon dioxide. Therefore the requirements for the pressure chamber where set to:

- A pressure resistance up to 15 MPa.
- A temperature range from – 60 °C to 40 °C.
- The possibility to observe the process inside of the chamber through a sight glass.

The high-pressure resistance was chosen because of the pressure that can occur in the interstice between tool and sheet metal during the forming process. The simulation showed possible temperatures below – 50 °C caused by the expansion and evaporation of the liquid carbon dioxide. The upper temperature was chosen because of the maximum temperatures that can arise in the tool during the forming process. These requirements were fulfilled by the *Büchi Midiclave Typ 4/1.0lt* (Uster, Switzerland; financed by the DFG).

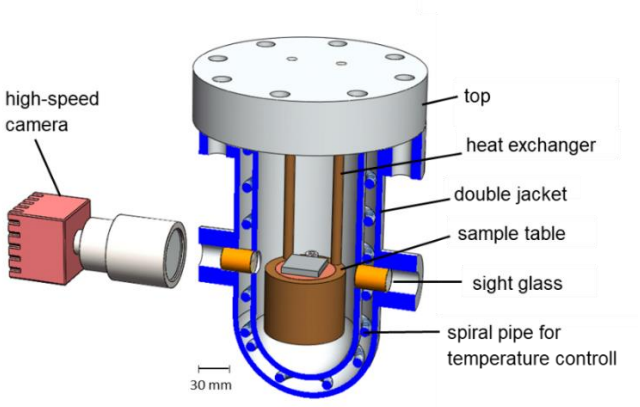


Fig. 19: Cross section of the pressure chamber. Adapted from [22].

Fig. 19 shows the cross section of the pressure chamber. The cladding is performed as a double jacket with a spiral pipe for temperature controlling (can temper the media inside of the pressure chamber). The sample table is connected to a second temperature controller for tempering the model of the tool with a micro hole inside. Thus, the tool temperature and the temperature of the carbon dioxide can be set individually.

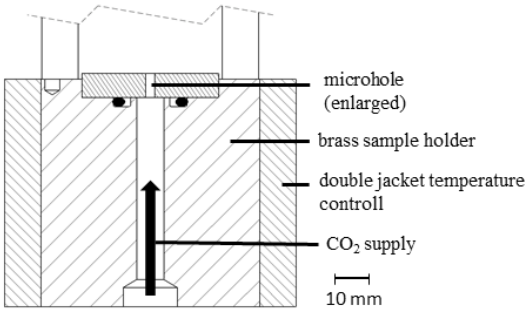


Fig. 20: Cross section of the sample table inside the pressure chamber. [23]

In Fig. 20, a cross section of the sample table inside of the pressure chamber can be seen. From the gas cylinder, the lubrication fluid flows through a pipe system directly to the bottom of the sample holder. In the case of carbon dioxide, a riser pipe inside of the gas cylinder is used. Thus, the $CO_2$ stays in the liquid state until the entrance of the micro hole. Due to the temperature control of the sample holder, it is possible to simulate different temperatures of the tool, which can occur during the deep drawing process.

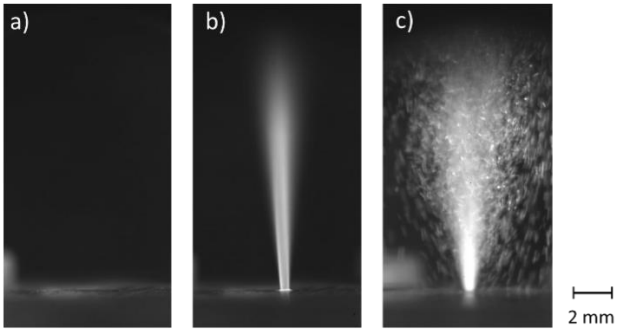


Fig. 21: Fountains of carbon dioxide after the exit of laser drilled micro holes in different aggregate states: (a) gaseous, (b) solid and (c) liquid.

As mentioned in connection to the CFD simulations, the expansion of the liquid $CO_2$ inside or after the exit of the micro hole leads to a cool-down. This phenomenon is called the Joule-Thompson effect. It is based on the van der Waals forces between the particles of the fluid. If single particles get more space, their motion becomes slower and the temperature drops. The substance-specific Joule-Thompson coefficient for $CO_2$ at ambient conditions is 1.1 K $bar^{-1}$ [24]. Beside this effect the liquid carbon dioxide evaporates partially. To overcome the intermolecular reactions, the enthalpy of vaporization is needed – the temperature drops. The combination of these two incidents lead to a drastic cool down of the medium to temperatures around – 78°C. At this temperature and atmospheric pressure, the carbon dioxide exist in its solid state (see Fig. 4). As shown in Fig. 21 the dry ice in the shape of small flakes arises. At further distance to the exit of the micro hole the dry ice sublimates

– it converts directly into the gaseous state. To clarify the phase state of the carbon dioxide during the deep drawing process, the pressure chamber was used to emulate the pressure, which occurs in the interstice between tool and sheet metal. Besides the pressure, the influence of the micro hole geometry as well as the tool temperature were investigated. Fig. 22 shows a comparison of the two different micro hole geometries at the same pressure and temperature level. At low chamber pressures the carbon dioxide escapes in its solid state, independent of the micro hole geometry. However, a different appearance of the fountain of the confuser and diffuser could be obtained. The fountain of the confuser is lower and wider in comparison to the diffusers fountain. With regard to the production of dry ice, the diffuser showed a higher amount of white in its fountain and an accumulation of dry ice around the micro hole. This leads to the conclusion that through the usage of the diffuser geometry a higher dry ice production can be reached. This corresponds to the results of the CFD simulations. At high chamber pressures the carbon dioxide escapes in its liquid phase, so no phase change occurs but the surface gets wetted with liquid carbon dioxide before a fountain appears. Concerning to the influence of the tool temperature and the chamber pressure a comparison is shown in Fig. 23. To sum the results of diffuser geometry up, the investigations showed a higher production of dry ice at lower tool temperatures. In addition it became clear, that the higher the pressure the more liquid carbon dioxide evaporates. [4], [23]

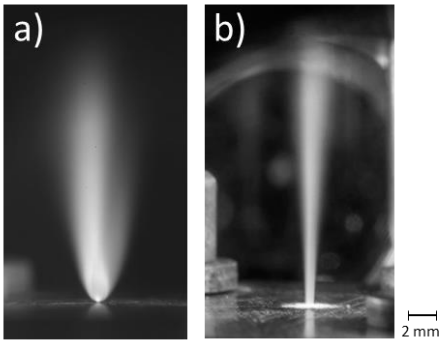


Fig. 22: $CO_2$ fountain of confuser (a) and diffuser (b) geometry, at the same pressure and temperature level. According to [23].

For further information about the fluid flow behaviour, a modified optical strip drawing test was carried out (see chapter 5.1.3).

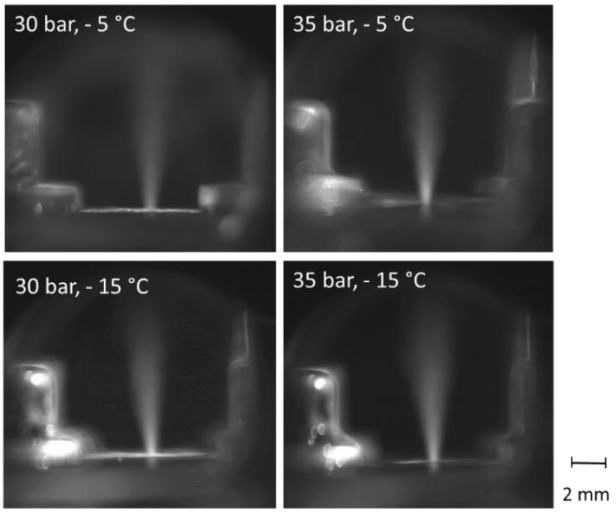


Fig. 23: Impact of temperature and chamber pressure on the $CO_2$ fountain.

In addition to the investigations of the stream out behaviour of carbon dioxide in the pressure chamber, different material surfaces were tested on wetting properties with liquid $CO_2$. To examine the wetting with liquid $CO_2$ the captive bubble method was used. Therefore, a sample is attached horizontally to the sample holder in the pressure chamber. Subsequent the chamber was flooded with liquid $CO_2$. With a needle gaseous carbon dioxide, in form of a small bubble, was positioned at the lower surface of the sample. By using a high-speed camera, the shape of the bubbles under the sample were observed and conclusions of the wetting behaviour

drawn. With this examination method also the surface conditions of work pieces after different cleaning processes used in dry-metal forming were analysed. The results were discussed in comparison to results achieved with X-ray photoelectron spectroscopy (XPS) and infrared spectroscopy. [25]

## 5 Investigations of basic tribological behaviour regarding volatile lubrication

### 5.1 Flat Strip drawing tests

Flat strip drawing tests reproduce the tribological conditions between the component flange and the blank holder as well as the flat areas of the die during deep drawing processes. For the tests performed in research project presented here, the strip drawing rig of the IFU was modified in such a way that the volatile lubricants could be injected into the contact zone between sheet metal material and the drawing jaw. The set-up of the testing rig is shown in Fig. 3. In order to ensure media supply, the strip drawing jaws were designed in two parts. Via feeding channels integrated into the upper part of the strip drawing tool, the medium is first led into a supply chamber inside tool, in order to be subsequently distributed to the micro holes of the lower tool part and thus to be introduced to the friction surface. Number, arrangement and geometries of the micro holes could be changed by using different lower tool parts. This allowed the influence of a large number of parameter combinations on the friction behaviour to be investigated. In the course of the investigations of the three funding periods, the geometry of the friction jaws was continuously optimised due to the findings gained with regard to rigidity, tilting stability and elastic deformation caused by the internal media pressure. In summary, the influence of the following parameters on coefficient of friction (COF) was investigated:

- Number of micro holes
- Arrangement of micro holes
- Used volatile lubricant
- Geometry of micro holes
- Normal contact pressure
- Different structured drawing jaws

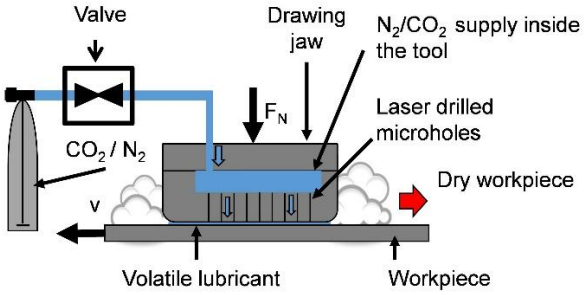


Fig. 24: Setup of the modified flat strip drawing testing rig. According to [4].

In the following, an overview of the knowledge gained from the extensive strip drawing tests is given.

#### 5.1.1 Influence of drawing velocity, surface pressure, number and size of micro holes on the coefficient of friction

The results of the flat strip drawing tests, in which $CO_2$ was used as volatile medium and drawing velocity, surface pressure, micro hole diameter as well as the number of micro holes were varied, are shown in Fig. 25. The black coloured error bars show the maximum and minimum measured values of the COF. Even though the scatter of the testing data is considerable at the low surface pressure of 2.2 MPa, it is apparent that the coefficient of friction decreases significantly with increasing number and diameter of the micro holes. Compared with the reference tests using mineral oil based lubricants (illustrated by the upper yellow box), the coefficient of friction is distinctly lower when using $CO_2$. At higher surface pressures of 5.8 and 9.0 MPa, the friction in the strip drawing test using $CO_2$ is also far below the reference values obtained with conventional lubricants. In comparison to the low surface pressure (2.2 MPa), however, the influence of the number of micro holes on the coefficient of friction is reduced at the higher surface pressures (5.8 and 9 MPa). This is due to a smaller gap between the two contact surfaces, caused by higher normal contact pressure. The smaller gap reduced the outflow rate of the volatile lubricants and therefore increasing the aerostatic load-bearing effect when using less numbers or smaller diameter of micro holes. This is also defined as sealing effect. These

results are beneficial for the design of a dry forming tool, since only few micro holes are required in areas with high surface pressure. Chosen drawing velocity was 50 mm/s and 100 mm/s and correspond to usual drawing velocities of deep drawing processes. Drawing velocity at normal contact pressures of 5.8 MPa and 9.0 MPa had only a very low influence on COF and not a clear tendency can be observed. Error bars at 2.2 MPa are too large for interpretations on the influence of drawing velocity either.

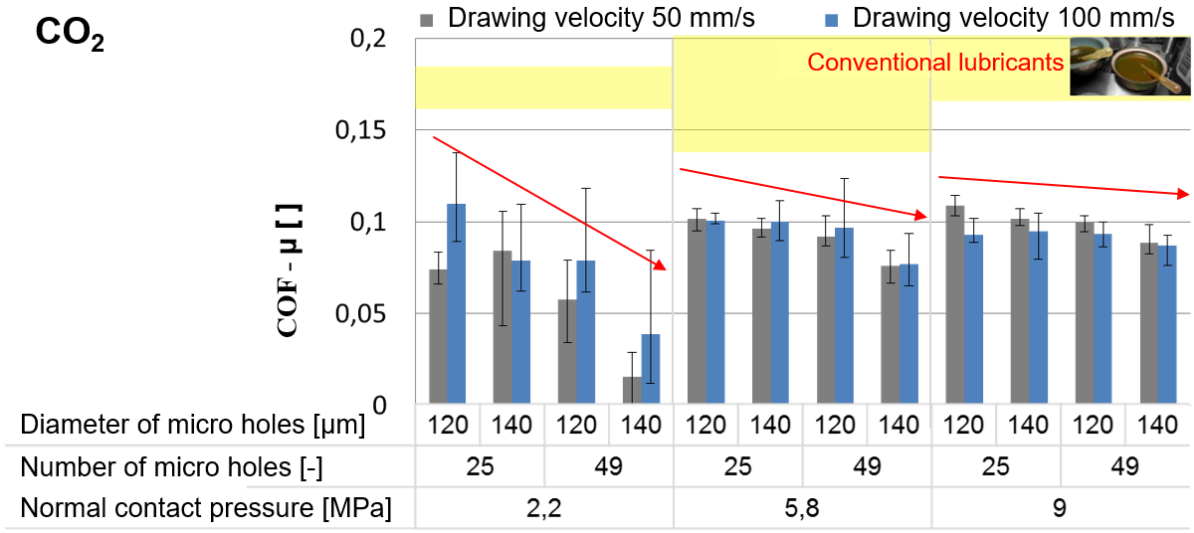


Fig. 25: Results of flat strip drawing tests using $CO_2$ and conventional mineral oil based lubrication. According to [26].

Additional flat strip drawing tests have been conducted using gaseous nitrogen as volatile lubricant. The coefficients of friction resulting from this investigations are depicted in Fig. 26. It is apparent that the scatter of testing data represented by the black error bars is again substantial at the surface pressure of 2.2 MPa. It could be observed, that low normal surface pressure combined with high gas pressure leads to unstable contact conditions. Reducing the error bars for a surface pressure of 2.2 MPa can be obtained in two ways, using a low number of micro holes with a small diameter (lowest flow rate) as well as using the max. number of micro holes with the largest diameter (max. flow rate).

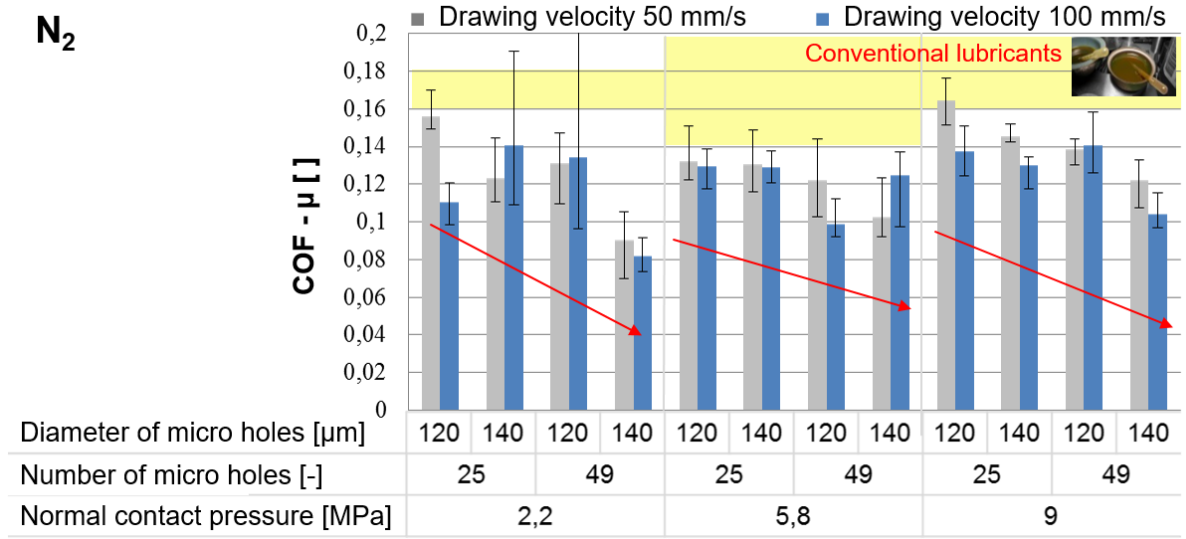


Fig. 26: Results of flat strip drawing tests using $N_2$- and conventional mineral oil based lubrication. According to [26].

The lowest COF can be obtained using parameter set for highest flow rate of $N_2$, which leads to a good separation of both, tool and sheet metal specimen. Despite the scattering of data, there is a tendency for the coefficient of friction to decrease with increasing numbers and diameter of the micro holes for the entire range of surface pressures examined, which also can be explained by an aerostatic load-bearing effect. In general, all averaged coefficients of friction determined using $N_2$ in the strip drawing tests are below the reference values of mineral oil based lubricants, but not as low as with $CO_2$ as lubrication. Drawing velocity have only a very

low influence on COF and not a clear tendency can be observed, because value range of the error bars exceeds the difference of the calculated mean values of the COF.

### 5.1.2 Further investigations on the influence of the micro hole design on the coefficient of friction

Based on the flat strip drawing results of the first funding period presented in the previous chapter, it was shown that the friction conditions in the novel tribological system are significantly dependent on the design of the micro hole geometry and the micro hole arrangement. This applies both, to $CO_2$ and $N_2$ as a volatile lubricant. For this reason, more detailed investigations were carried out with regard to the design of the micro holes in the second funding period, which are presented in this section.

In order to gain a better understanding of the interdependencies of the tribological system using volatile media as lubricant substitutes, an overview of the main effects of influencing parameters is presented here. The number of holes (3, 7, 9, 21) and the diameters of the micro holes (200 µm, 300 µm) and nozzle types (diffuser, confusor) were changed. The main effects of these parameters on the coefficient of friction are depicted in Fig. 27.

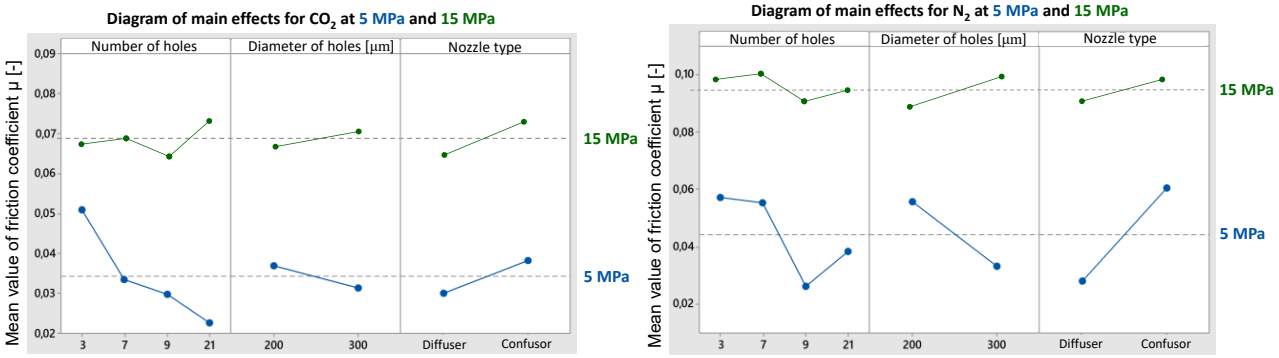


Fig. 27: Main effects of different micro hole parameters on the COF determined by flat strip drawing tests and DC05+ZE sheet metal specimen. [13]

When using nitrogen ($N_2$) or carbon dioxide ($CO_2$) as lubricants, a significant reduction in the coefficient of friction is achieved at low contact pressure (5 MPa) with an increasing number of micro holes. The tests using $N_2$ and 21 micro holes represent an exception to this, as friction increases slightly compared to the tests using $N_2$ and 9 micro holes. Reason for this is that the pressure in the supply channels decreases substantially with a larger number of holes due to the increased outflow of the gaseous $N_2$. Thus, a lubricating effect is only achieved in a weakened manner. $CO_2$ is not as sensitive to high outflow rates (large diameters combined with high number of micro holes), since the specific volume increase at 20°C is almost four times higher than for $N_2$ due to the phase change from liquid to gaseous. For both fluids, diffusers achieve lower friction coefficients at both 5 MPa and 15 MPa. These results were used, among other things, for the design of the forming tool of the rectangular cup, in which all laser-drilled micro holes were designed as diffusers [27]. Dashed lines in both diagrams in Fig. 27 represent the averaged value of all friction coefficients obtained by the flat strip drawing experiments at a contact pressure of 5 MPa and 15 MPa. As can be seen, lower averaged friction values can be achieved with $CO_2$ than with $N_2$ at both, high and low contact pressures.

### 5.1.3 Results optical strip drawing test regarding the phase change of $CO_2$

In order to investigate, if the $CO_2$ is in solid, liquid or gaseous phase during a deep drawing process and if there is a correlation between the phase of the $CO_2$ and the coefficient of friction, the same tools for conventional strip drawing tested under the same pressure conditions in the new designed strip drawing test. The tool was pressed on the glass pane by the pneumatic cylinder. Before the tool was in contact with the glass, the $CO_2$ was switched on, whereby a free escape of the $CO_2$ occurred at the beginning. When the adjusted surface pressure was achieved, the high speed camera was turned on and the sledge with the integrated glass window was drawn with constant velocity underneath the tool. In Fig. 28, the pictures captured with the high speed camera are shown for both tools and a surface pressure of 5 and 10 MPa at a drawing distance of 0, 5, 10, 15, 57.5 and 115 mm, respectively. The dry ice is displayed as white pixels.

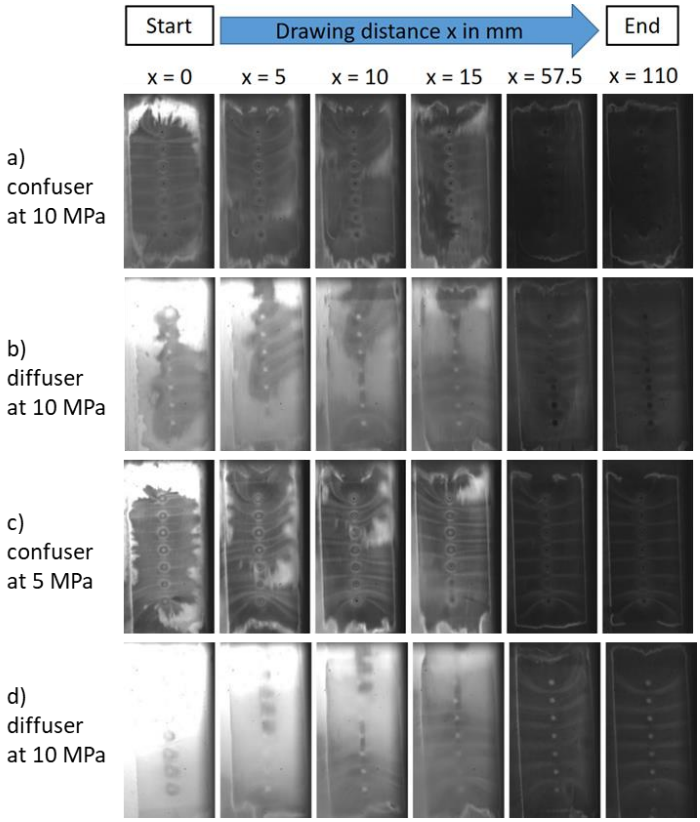


Fig. 28: White amount during the movement for x = 0, 5, 10, 15, 57.5 and 115 mm a) Tool 1: Confuser, 10 MPa; b) Tool 2: Diffuser, 10 MPa; c) Tool 1: Confuser, 5 MPa; d) Tool 2: Diffuser, 5 MPa. According to [7].

To compare the different picture quantitatively, the average pixel greyscale was calculated for each picture insight a ROI. In general, every pixel on the captured pictures is displayed by a pixel value between 0 (black) and 255 (white). Thus, a high mean greyscale value is synonymous to the existence of a high amount of dry ice in the contact zone, whereas no solid $CO_2$ exists at a mean greyscale value of zero. By plotting the mean greyscale against the drawing distance in a diagram, the change in formation of solid $CO_2$ can be analysed (see Fig. 29).

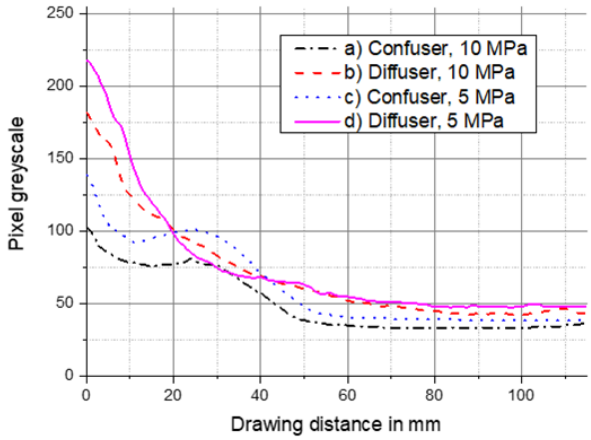


Fig. 29: Mean value for the grayscale dependent on drawing distance for different nozzle shapes and surface pressures. [7]

Due to the free outpouring of the $CO_2$ at the beginning, an increased formation of $CO_2$ snow can be detected for all experiments at starting time. Especially for the diffuser, a high amount of dry ice is found between the tool and the glass at the start of the drawing (see first picture of Fig. 28 especially b and d). When the movement of the sledge starts, the solid $CO_2$ is pushed out of the contact zone and less new ice is produced. The mean pixel greyscale value declines for all experiments. Constant drawing conditions occur at around 60 mm drawing distance.

Inside the forming zone, a mixture of different phases occurs as long as the valves are open and the $CO_2$ flows out of the micro holes. There is a $CO_2$ snow formation visible, but not over the whole contact zone. The ratio between the solid and gaseous phase shifts in the direction of the gaseous one during the movement. From the p-T-diagram (Fig. 4) for $CO_2$, it can be seen that once solid $CO_2$ is formed, it does not become liquid again by warming. It sublimes directly into the gas phase. It is to be assumed that mainly a mixture of solid dry ice and gas lubrication exists during the real deep drawing process.

In general, each micro hole produces dry ice in different amounts. The higher the surface pressure, the less $CO_2$ snow can be formed. Independent of the surface pressure, a diffuser is able to form more $CO_2$ ice as a confuser. CFD simulations (see chapter 2) and pressure chamber tests support the observation that a diffuser can form more $CO_2$ snow with similar conditions as a confuser. Within a diffuser, a compressor shock occurs during the through-flow, which implies a sudden increase in temperature and pressure. This promotes the formation of $CO_2$ snow inside the diffuser. In the simulation of the confuser, such a compression does not exist. The formation of $CO_2$ snow inside this micro hole shape is thus unlikely. Only directly at the outlet, the formation will occur.

Comparing these results with the measured coefficient of friction in the conventional strip drawing test, a correlation between friction behaviour and amount of formed $CO_2$ ice can be found. A diffuser produces more dry ice than a confuser and the measured coefficient of friction is lower. A diffuser as well as a confuser can produce more dry ice at a lower pressure (5 MPa) than at a higher pressure (10 MPa). It could be assumed that the existence of solid $CO_2$ is beneficial for the friction behaviour in the drawing process. The correlation between the measured coefficient of friction and the amount of dry ice in the contact zone is showed in Fig. 30. The average greyscale value of the captured picture for the drawing distance between 60 and 100 mm is used as parameter for the amount of dry ice. The friction decreases by having more dry ice in the contact zone for a contact pressure of 5 MPa. Though this effect is less clear, the friction also decreases with an increasing ice amount for a contact pressure of 10 MPa. It seems that dry ice reduces the friction by using $CO_2$ as volatile lubricant.

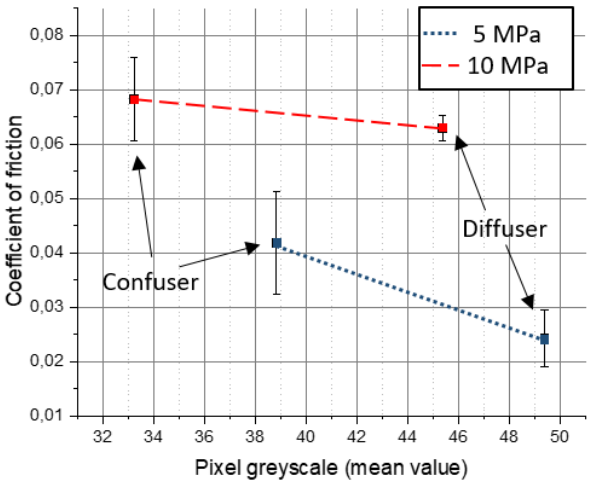


Fig. 30: Correlation between the coefficient of friction and produced amount of dry ice results in an average greyscale value for a drawing distance between 60 and 100 mm. [7]

Fig. 30 shows that the existence of dry ice at different pressure levels influences the friction behaviour to varying degrees. In accordance with deep drawing using mineral oil based lubricants, the surface pressure has a main influence on friction. It is assumed that the reduction of the real surface pressure in the interstice between tool and sheet metal influence the friction behaviour due to the load capacity of the $CO_2$ caused by aerostatic pressure. [7], [13]

### 5.1.4 Investigation on the influence of structured tools on the coefficient of friction

The general motivation for the investigation of the influence of structured tools was the optimisation of the outflow conditions and thus the improved dispersion of the volatile lubricants used in the contact zone. For this purpose, different laser structuring methods were examined for their friction-reducing effect by means of flat strip drawing tests. A star-shaped structure (*), a cross-shaped structure (#) and a drop-shaped structure (<, >) were used. Last one was tested in both drawing directions.

### 5.1.4.1 Laser surface structuring

Recent developments in ultrashort pulse laser sources offer the ablation of metals without any melt left in the irradiated area. The use of ultrashort laser pulses is highly beneficial, as the melted rim, commonly seen in short pulse laser processing, which acts as an asperity to increase friction, is avoided. In addition, the depth and width of the structures can be adjusted to the requirements by applying a set of proper laser parameters.

The star- and cross-shaped structures were produced by using a scanning optic from Scanlab to move a focused laser beam across the sample surface. Examples of both structures are shown in Fig. 31 a) and b) respectively.

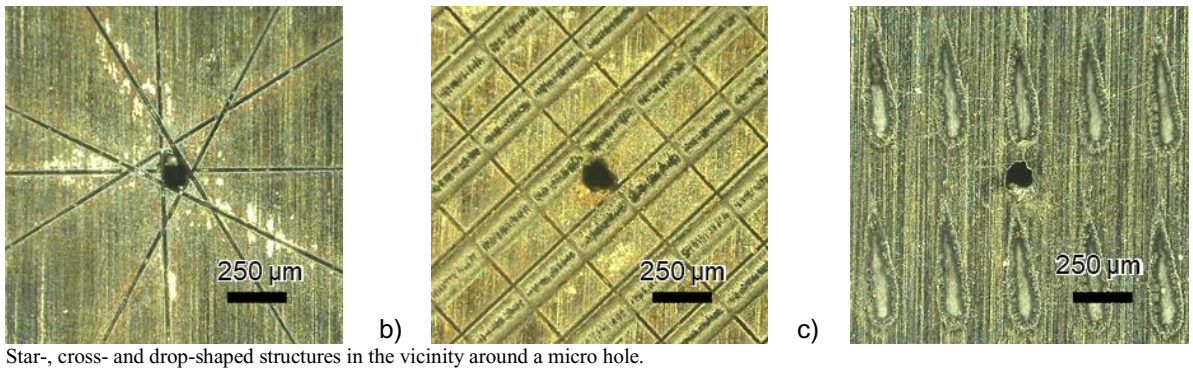


Fig. 31: Star-, cross- and drop-shaped structures in the vicinity around a micro hole.

A different approach was taken to produce the drop-shaped structure (Fig. 32 c). By intentionally passing the raw laser beam de-centrally through a bi-convex focussing lens, the effects of astigmatism and coma aberration were used to create a drop shaped beam profile on the sample surface. The schematic representation of the optical setup and the spot diagram is shown in figure Fig. 32 a) and b). In addition a 3D-image measured with a laser scanning microscope is shown in Fig. 32 c).

All structures were produced using picosecond pulses with the pulse energy of 250 µJ and the repetition rate of 20 kHz.

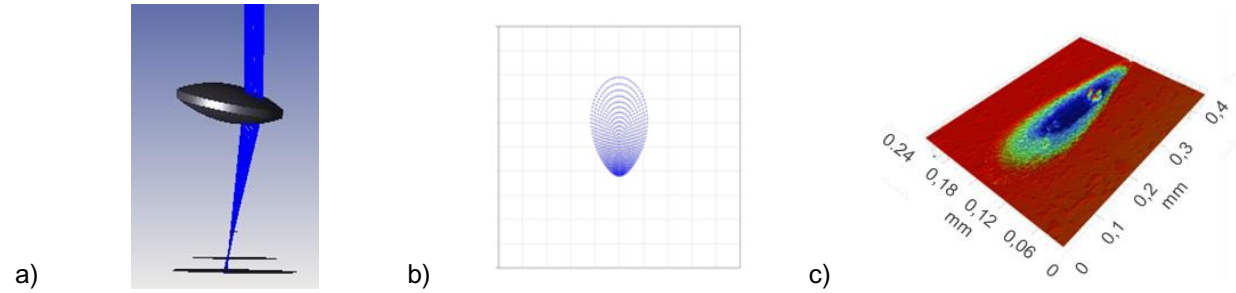


Fig. 32: Drop-structure; a) schematic representation of the optical setup; b) simulated spot diagram on the sample surface; c) 3D image measured with a laser scanning microscope.

### 5.1.4.2 Results of strip drawing tests with structured jaws

Based on the flat strip drawing tests with unstructured jaws, it has been investigated whether the outflow conditions and thus the dispersion of the volatile lubricants injected in the contact zone can be beneficially influenced by the tool´s surface structure. For this purpose, different laser structures were examined for their friction-reducing effect. These examinations included a star-shaped structure (*), a cross-shaped structure (#) and a drop-shaped structure (<, >). The latter structure was tested in both drawing directions, forward and backward. All kinds of structured surfaces are depicted in Fig. 33.

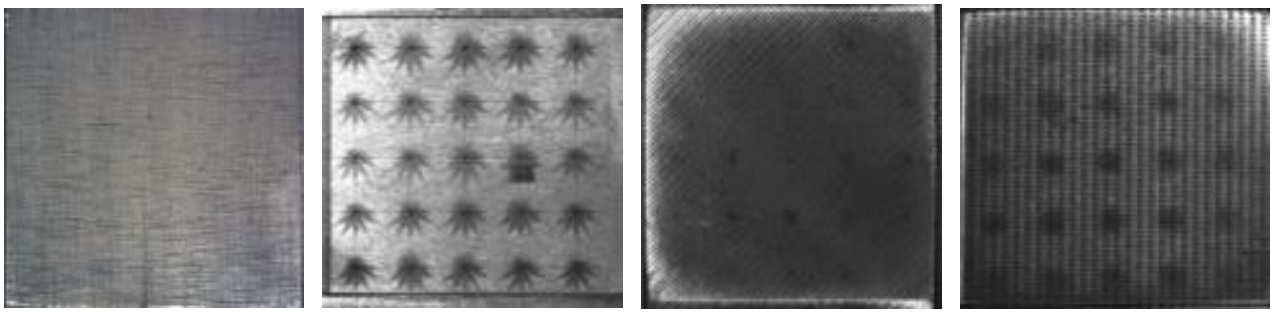

Fig. 33: Different kinds of surfaces of laser structured drawing jaws with 25 micro holes. From left to right side: unstructured, star-shaped, cross-shaped and drop-shaped structure.

All strip drawing tests were repeated 5 times at 100 mm/s drawing velocity and the surface pressure was set to 5.8 MPa, as these parameters represent values of a standard deep drawing processes using steel sheet metal specimens. For evaluating the influence of the different surface structures on the COF, strip drawing jaws having 9, 27 and 49 micro holes were manufactured and tested subsequently. Afterwards, these test results were compared to the investigations without jaw structuring already presented above, as shown in Fig. 34.

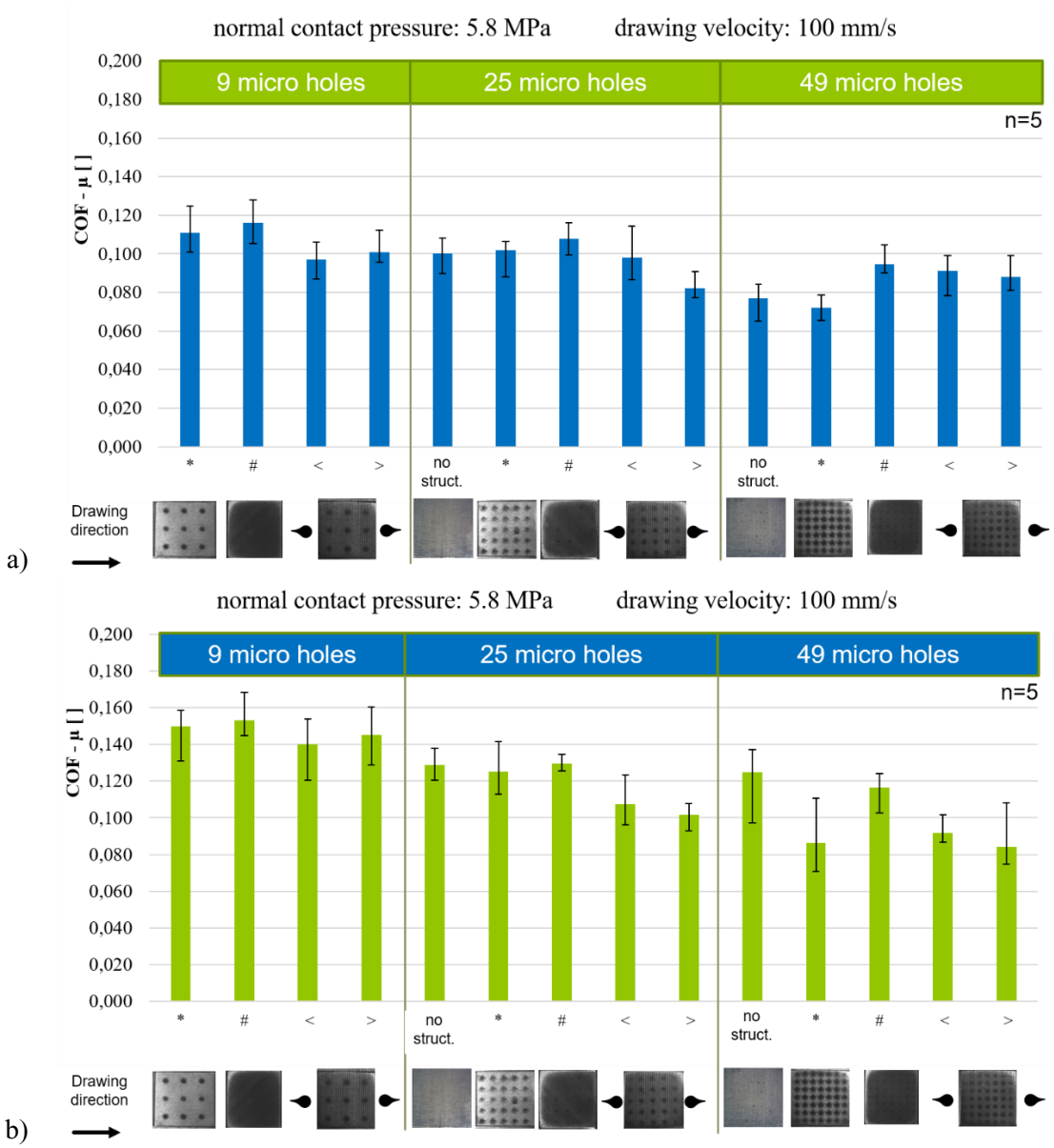


Fig. 34: Influence of different microstructures on the coefficient of friction for $CO_2$ (a) and $N_2$ (b).

As can be seen in Fig. 34, there is no significant friction reduction for $CO_2$ due to surface structuring on the drawing jaws (approx. ±0,01). The cross-structure even increases the friction in all cases. When using $N_2$, a slight friction reduction can be measured with the star and drop structures. Here, the drop-shape structures does not show a clear difference in the friction coefficient when changing the drawing direction. However, the tests revealed a high risk of adhesions and micro-ploughing due to the sharp edges of the surface structures, which would considerably impair reliability of dry forming processes. Additional CFD simulations of basic structures in the contact zone showed the same tendency, which is described in more detail at the end of chapter 2. For this reasons, surface structures of tools were no longer considered in the further investigations.

## 5.2 Impact of hard coatings on coefficient of friction and wear

In addition to the lubrication with carbon dioxide or nitrogen, a hard coating was applied to the tool. This subsequent deposited layer should improve the tool life. An additional reduction of the friction coefficient might be conceivable. Therefore, especially investigations with liquid $CO_2$ and two different types of hard coatings deposited on 1.2379 tool steel were made.

### 5.2.1 Silicon nitride coating

$Si_3N_4$ as a non-oxide ceramic material has several positive material properties. Besides the low density (3.44 g $cm^{-2}$), it has a very high fracture toughness and at the same time good flexural strength (> 800 MPa at 20 °C). Due to the inherent microstructure a high thermal shock resistance is given. These properties make silicon nitride insensitive against shocks and impacts. Hence, $Si_3N_4$ is commonly used for tools in mechanically harsh environments. For producing the silicon nitride coatings, a plasma-enhanced chemical vapour deposition (PECVD) process with an inductively coupled plasma (ICP) source was applied. As precursor and process gas monosilane and ammonia were used in a mixture ratio of 1:10. The process duration was 10 minutes with a power input of 2 kW and a process pressure of 0.2 µbar.

### 5.2.2 Hydrogenated amorphous carbon coating

The a-C:H:W/a-C:H coating consists of a multi-layered design with a total coating thickness of 2.2 µm as shown in Fig. 35. First, a thin Cr layer of a few nanometers and a $CrN_X$ coat with increased hardness was deposited acting as a bonding agent. To increase the adhesion strength further between substrate and functional layer a graded $(Cr,W)C_y$ and a-C:H:W intermediate layer was deposited. This step realizes the smooth transition between metallic and non-metallic character. Finally, a hard-functional a-C:H of about 22 GPa $HIT_{0,001}$ was applied. Thus, a low dry friction coefficient and high wear resistance can be ensured.

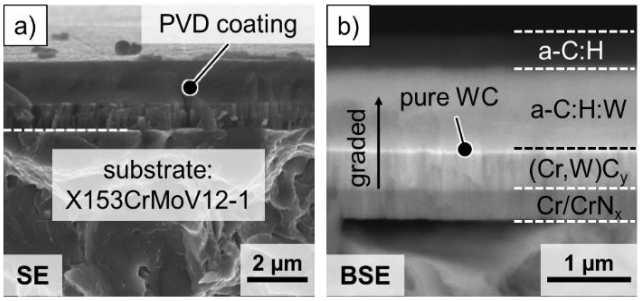


Fig. 35: SEM fracture patterns of the a-C:H:W/a-C:H coating system: (a) SE image and (b) BSE image. [28]

The hydrogenated amorphous carbon coating was produced via reactive magnetron sputtering at the Leibnitz Institute for Materials Engineering (IWT) in Bremen. For the reactive magnetron sputtering a target material is vaporized due to a momentum exchange caused by ionized process gases. As process gases the noble gases argon and krypton are used.

### 5.2.3 Results of strip drawing tests with coated jaws

To evaluate the effect of the hard coatings on the friction coefficient, strip drawing tests were carried out. For these investigations, the experimental setup explained in chapter 5.1 was used. To include the impact of the surface pressure, two different loads (5 MPa and 15 MPa) were tested. For an averaged friction coefficient, only values with stationary behaviour in the middle of the drawing distance were considered. Fig. 36 shows

the measured coefficient of friction of the different coated exchangeable jaws in comparison to an uncoated jaw.

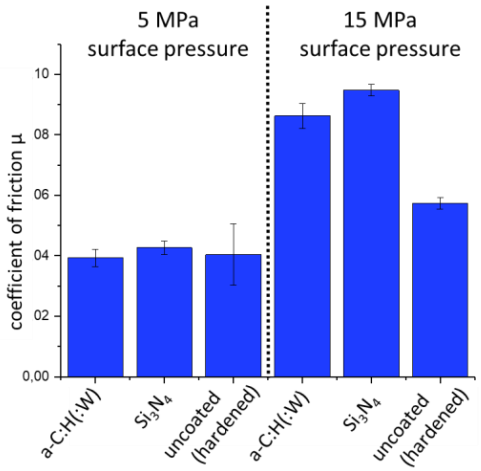


Fig. 36: Representation of the coefficient of friction for coated and uncoated exchangeable jaws, each tested with 5 MPa and 15 MPa surface pressure. [29]

For a surface pressure of 5 MPa, all three tools are at the same low friction level. Only at a surface pressure of 15 MPa, the coated exchangeable jaws showed a higher coefficient of friction compared to the uncoated one. This can be attributed to excessive wear of the surface around the micro holes. As shown in Fig. 37 the silicon nitride coating as well as the carbon coating got deep wear scars in drawing direction originating from the micro holes. A replacement of the coating especially around the micro holes can be observed. The replaced particles of the coating act like an abrasive grit. Hence, the high coefficient of friction measured with the coated jaws is with high probability caused by defects, which are triggered by debris formation around the micro holes. For further investigations with coated tools, an improved geometry of the micro hole exit as well as an enhanced coating design must be implemented. [29]

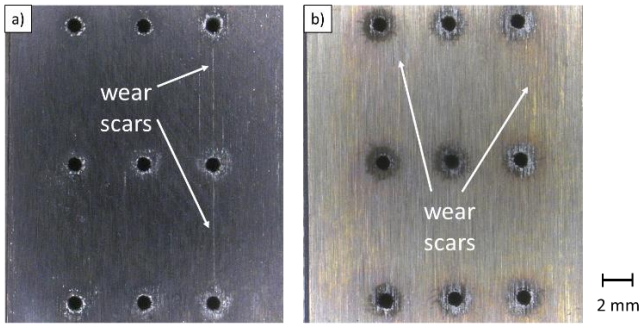


Fig. 37: Wear scars and wear around the micro holes using the two tested coating systems: (a) Hydrogenated amorphous carbon coating and (b) silicon nitride coating. [29]

### 5.3 Stretch-bending investigations

In order to characterize the novel tribological system in the area of highly loaded tool radii occurring, for example, at die entry radii, a stretch-bending testing rig with integrated media supply has been established at IFU (see Fig. 38). With this system, strips of 60 mm width can be drawn over different radius sizes (R5 to R12.5) with a wrap angle of 90°. Here, hydraulic cylinders are used to pull the strip at a constant speed at one end and to hold it at the other end with a constant retention force. In this way, stationary friction conditions occurring at tool radii can be reproduced and the average friction at such areas can be determined experimentally using the acting tension and retention forces. The tension and retention forces are measured using integrated piezo load cells. Finally, the radial friction can be calculated using friction equation according to Euler/ Eytelwein.

In the investigations carried out with this testing rig, the influence of the injection angle, the radius size, the retention force and the micro hole arrangement on the friction conditions at tool radii were analysed. DC05+ZE

was used as sheet metal material and $CO_2$ as lubricant substitute. Since initial stretch-bending-tests using nitrogen ($N_2$) as lubricant substitute have shown that zinc adhesions occur on the radius inserts, which even increase with decreasing radius size, the tests were conducted with $CO_2$ only. The investigation results obtained are discussed in the following chapters.

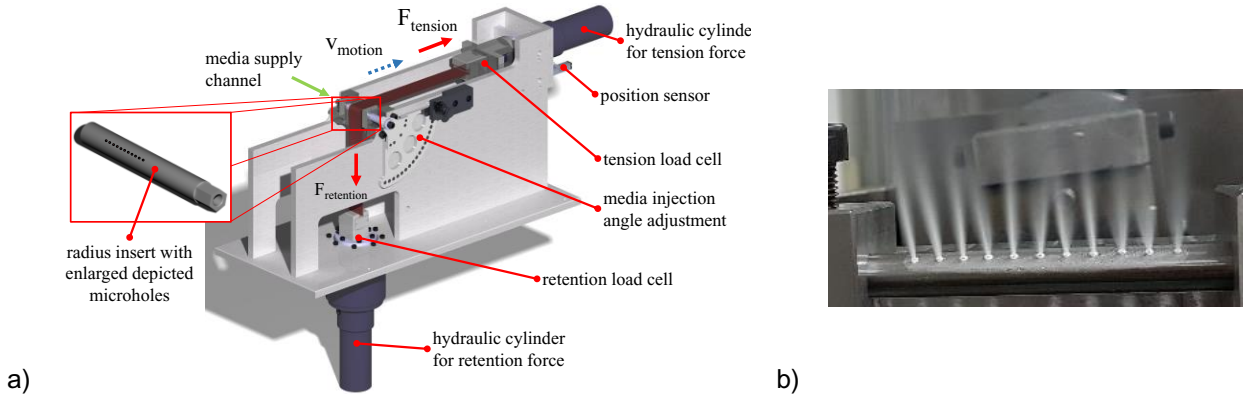


Fig. 38: Set-up of Stretch-Bending-Testing rig (a) and free flow out of $CO_2$ at radii with integrated laser drilled micro holes (b). According to [30].

## 5.4 Influence of injection angle on coefficient of friction

The aim of the investigations described in this subchapter was to determine optimum injection angles of the volatile lubricant in high loaded tool radius areas in order to achieve lowest coefficients of friction. The injection angle α was changed in the course of these investigations between 30° and 60° in steps of 5°. The results obtained are shown in Fig. 39. As can be seen in the diagram, an optimum range of injection angles could be determined independent of the restraining forces and thus the corresponding surface pressures. The injection angles achieving lowest coefficients of friction range between 40° and 45°.

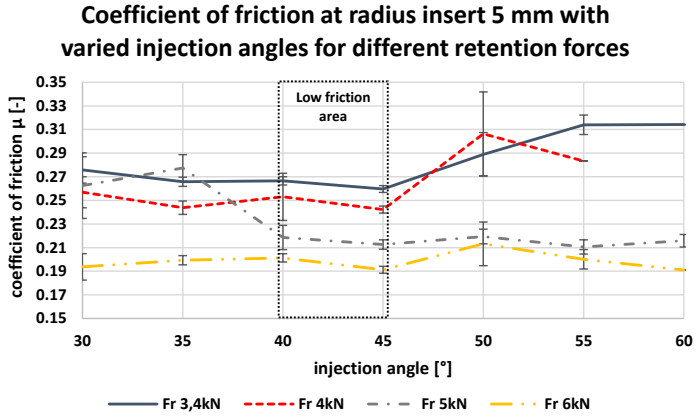


Fig. 39: Optimization of coefficient of friction for different injection angles using $CO_2$ at different retention forces. [30]

The results of the experiments performed with retention forces ($F_r$) of 3.4 kN and 4 kN show same tendencies. Here, the coefficients of friction remains relatively constant at small injection angles. Hence, at these lower retention forces, the volatile medium can be introduced into the gap between tool radius and sheet metal strip at an angle between 30° and 45° without significantly affecting the friction conditions. However, if the medium is injected in angles greater than 45° at these retention forces (3.4 and 4 kN), a significant increase in friction can be noticed. During the tests, this was also noticeable by the occurrence of zinc adhesions on the radius inserts. The occurrence of these adhesions also caused the relatively high scattering of the coefficients of friction determined at these larger injection angles values. For the same reason, the experiments at a retention force equal to 4 kN were stopped at 55°. At a restraining force of 5 kN, an exactly reversed behaviour can be observed. Up to an injection angle of 35°, relatively high coefficients of friction were determined and from an angle of 40°, the values remained rather constant at approx. 0.22. It can therefore be assumed that with higher surface pressures a better sealing (gaseous lubricant) of the friction zone occurs, which has a positive effect on friction above an injection angle of approx. 40°. This behaviour is clearly evident with a retention force of 6 kN. Here, a constantly relatively low coefficient of friction occurs over the entire angular range of the injection angle.

## 5.5 Influence of radius size and retention force on friction behaviour

Fig. 40 provides an overview of the numerous investigations carried out with the SBT rig regarding the influence of different radius sizes on the coefficient of friction in the areas of tool radii. Here, all investigations were carried out using single-line arranged micro holes (see Fig. 41) and DC05+ZE sheet material and each parameter set was repeated three times at least. As stated before an injection angle of 45° has been found to be optimal for low friction coefficients and the prevention of adhesion formation. Therefore, all investigations presented were conducted using this setting.

When comparing volatile lubricants to the conventional mineral oil based reference lubricant (*Wisura ZO3368*), the diagram shows a reduction of the friction coefficient for almost all parameter combinations in which $CO_2$ was used. The coefficient of friction varies over all tests in a range from $\mu = 0.127$ to 0.288 and is considerably higher than in the case of the flat strip drawing experiments, where the friction coefficient did not exceed $\mu = 0.08$ when using $CO_2$. This is due to the higher normal contact pressures at tool radii compared to flat contact interfaces. Numerical investigations on the occurring normal contact pressures at the SBTs are currently in progress and will quantify this difference in more detail.

As can be expected from [31], increasing radius size leads to decreasing friction coefficients. As shown in Fig. 40, this not only applies for conventional mineral oil lubrication but also for $CO_2$ when using radius inserts R5, R7.5 and R10. As depicted in the figure, only the largest radius insert R12.5 shows a different behaviour when using $CO_2$. Here, the coefficient of friction remains on the same level of approx. $\mu = 0.13$ for all tested retention forces. This is probably due to two mutually influencing effects of the coefficient of friction. On the one hand, the friction of larger radii is reduced due to the reduction of the normal surface pressure. On the other hand, the friction surface increases at larger radii, which is accompanied by a reduction of the lubricating effect using $CO_2$. The balance of both effects is achieved at a radius of 12.5 mm.

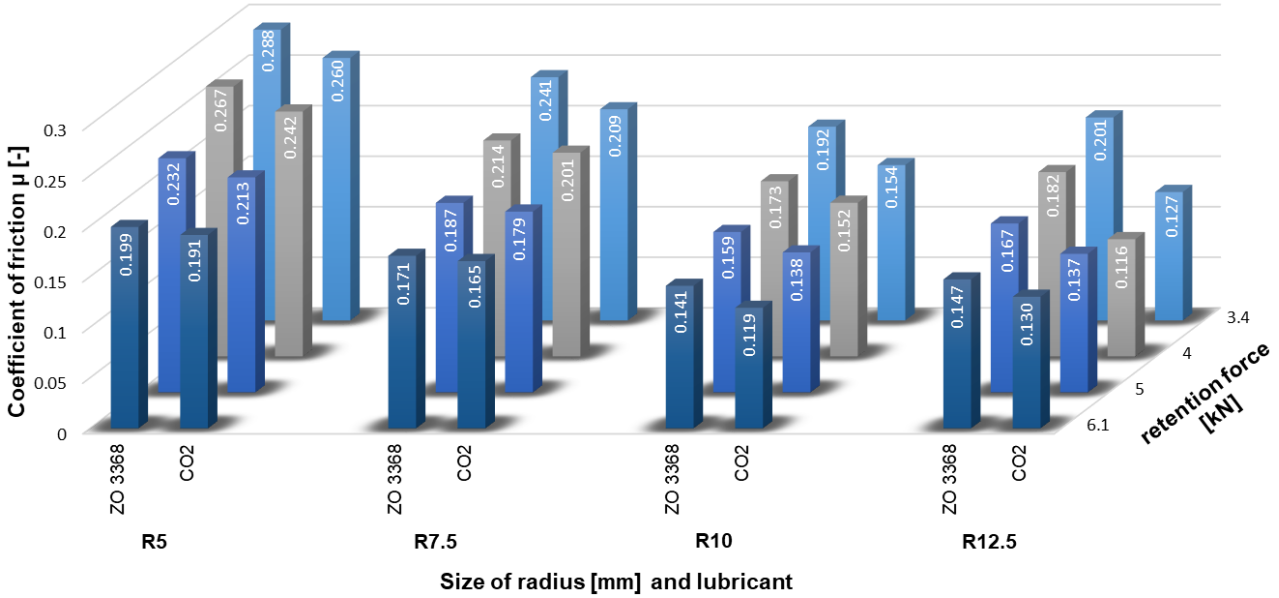


Fig. 40: Experimental results of stretch bending tests - sheet metal material DC05+ZE, injection angle 45° and single line arranged micro holes for $CO_2$.

## 5.6 Influence of micro hole arrangement on coefficient of friction

Several experiments using radius inserts with single-line arranged micro holes and injection angle deviating from 45° have shown adhesions, when using DC05 with or without a zinc coating as sheet material. Therefore, further radius inserts were manufactured with double-line arranged micro holes in order to address this issue (see Fig. 41).

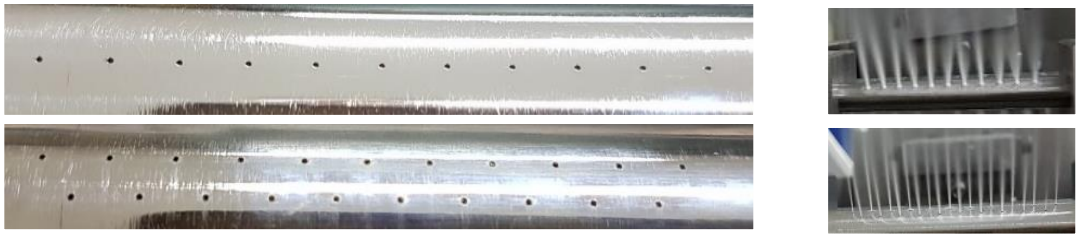

Fig. 41: Single and double-line arranged micro holes at tool radii used for SBTs.

As shown in Fig. 42, no significant difference between the results of the single-line and the double-line arrangement of micro holes could be noticed when using $CO_2$ and the radius R7.5. This is due to the lower normal surface pressure values compared to the radius R5, which showed differences of the COF up to a retention force of 5 kN. However, by using radius inserts with double-line arranged micro holes, adhesions at high retention forces could be avoided. Comparing the dashed curves for a 30° injection angle in Fig. 42 a) and b), gained results show an increase of the friction coefficient for the single-line arrangement at an retention force of 5 kN. This effect does not occur using double-line series. Even large error bars as those in Fig. 42 a), which arise from adhesion occurrence, are eliminated by using double-line arrangement.

In summary, a significant reduction of adhesion formation and a slight reduction of absolute friction coefficients could be achieved by increasing the number of volatile lubricants injectors. However, the results of radius insert R7.5 indicate that a saturation state of the required lubricant quantity was reached in this case by applying the second line of injectors. This can be observed in Fig. 42 c) and d) by the almost identical coefficients of friction for single and double-line arrangements. Thus, a further increase of the number of injectors would probably not further improve the tribological system.

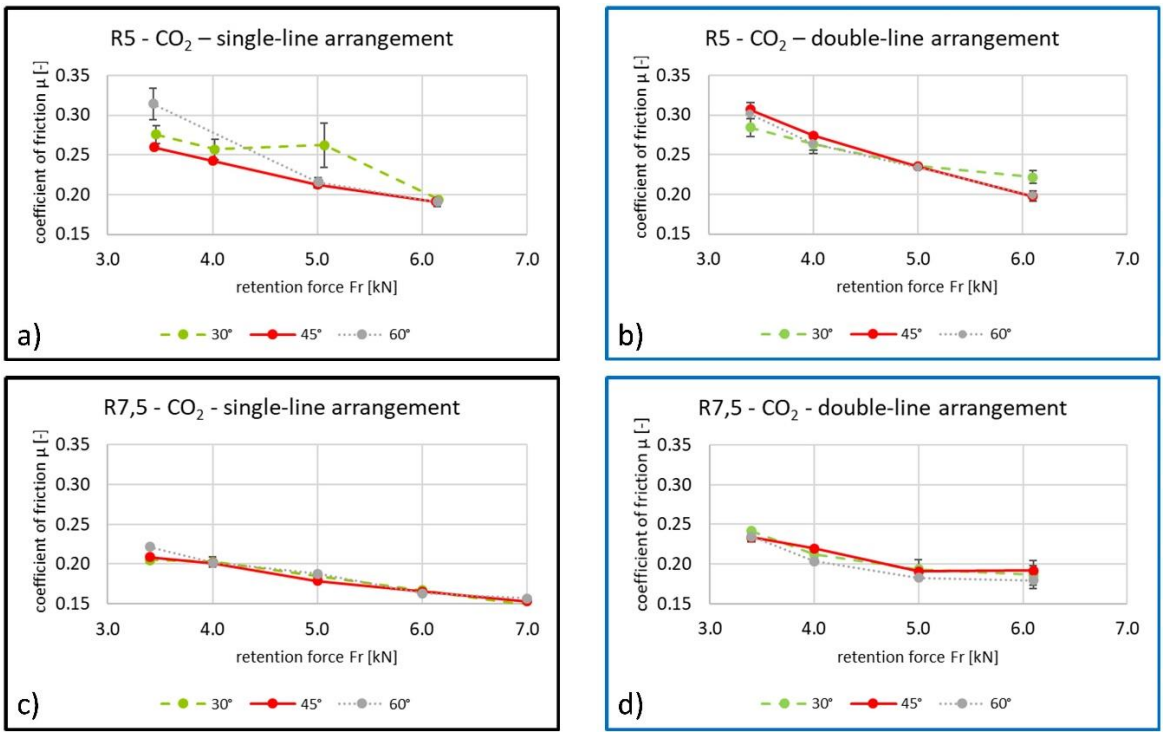


Fig. 42: Results of SBT (stretch-bending-test) - single and double-line arrangement of injectors. [20]

## 6 First realisation of novel tribo-system using the deep drawing process of a U-profile

For the first-time implementation of the new dry forming approach, the relatively simple forming process of a U-profile geometry was initially chosen. Here, the challenge was to design the valves, the valve control and the supply channels for the volatile medium at a pressure of 60 bar as well as the laser drilling of the micro holes. Fig. 43 shows a schematic sectional view of the tool active parts manufactured. The tool consists of two blank holders and dies each equipped with three feed channels for $CO_2$ or $N_2$ respectively. The volatile medium is introduced into the contact zone between the blank holder and the sheet metal and between the die and the

sheet metal via the laser-drilled micro holes. The media flow in the feed channels can be activated by one valve each. Since the relative movement between punch and sheet metal material is very small, there is no lubrication required at this point.

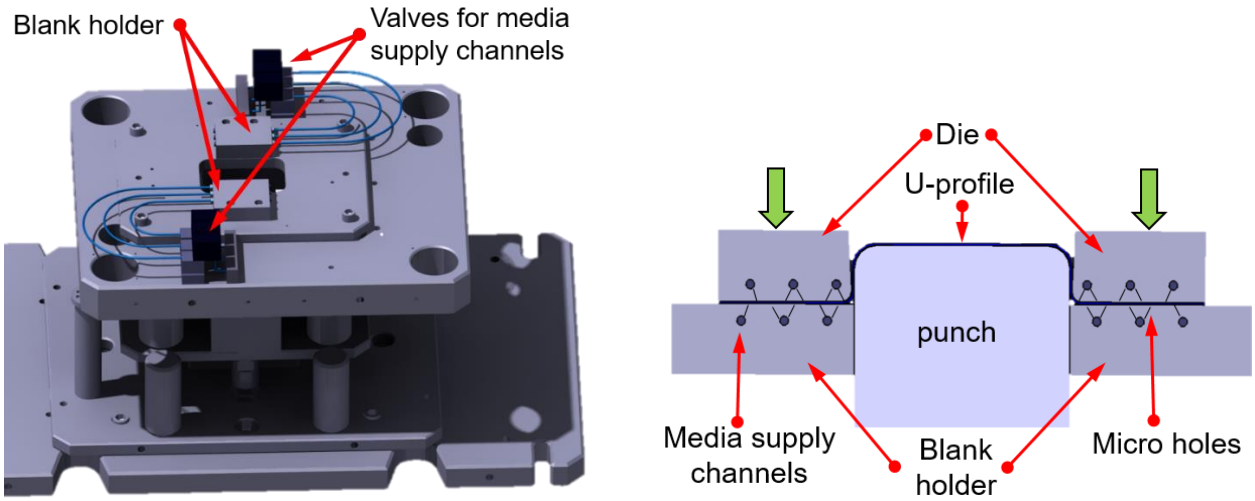


Fig. 43: Set-up for U-profile tool and principle of media supply.

Based on the results of the strip drawing tests presented above, a diffuser having a diameter of 200 µm at the transition to the feed channel and a diameter of 600 µm on the outlet side to the sheet metal material was chosen as nozzle type. Furthermore, a relatively high value of 10 mm was selected as distance between the single micro holes. For the drawing jaws used in the strip drawing tests, this distance was a maximum of 7.5 mm. The results of the investigations carried out with optical accessibility to the drawing jaw surface additionally showed that a staggered arrangement of the rows is useful, as this improves the flow out of the micro holes. This results in a number of 33 micro holes per blank holder. Since the contact area between the sheet metal material and the blank holder is 35 cm², the blank holder thus provides a micro hole coverage of 0.94 per cm². Furthermore, a series of micro holes are located in the area of the radius at an injection angle of 15°. This arrangement of only one row in the radius (15°) was chosen in order to ensure a free outflow of the volatile medium at this point only for a short time at the beginning of the forming process. After covering the micro holes at the draw-in radius with increasing drawing depth by drawing part, a free flow out of the volatile media is prevented and lubrication is ensured.

The 12 valves for activating media supply of the feeding channels in total are controlled by a valve control system developed in-house. Thus, the single valves can be individually switched on and off using *HBM's "Catman"* measurement software. The path of the press ram is used as the control variable. All valves are opened shortly before the ram is placed on the sheet metal material. In the following, the valves are switched off one after the other from the outside to the inside as the sheet metal material is drawn in, in order to prevent the $CO_2$ from flowing out freely.

First experiments using the developed tool were carried out without any lubricant, with the mineral oil-based reference lubricant *Wisura ZO3368* and with $CO_2$ lubrication at a speed of 5 strokes/min and a blank holder force of 50 kN. The same electrolytic galvanized sheet material DC05+ZE as in the strip drawing tests was used having a length of 225 mm and a width of 70 mm. Without lubrication, no U-profile could be drawn (see Fig. 44 left). On one side, the sheet was completely clamped, thus the draw-in of the blank was only performed on one side. Also by changing the starting position of the sheet metal material by several millimetres and thus reduce the surface pressure on the clamped side, drawing of the U-profile was not successful. Even when using the reference lubricant with a quantity of 1.5 and 3 g/m², no satisfactory result was achieved. Therefore, spotting ink was used to determine the contact surface between the tool and the blank and the associated local distribution of the surface pressure. An uneven distribution was found, which led to the clamping of the sheet metal material. Normally, the pressure distribution in the area of the blank holder is homogenized by spotting until a correct run-in path of the blank leads to good parts. However, before this was done, the new tribosystem was first tested with $CO_2$ as a temporary acting dry lubricant. Already during the first application, a U-profile could successfully be drawn (see Fig. 44 right).

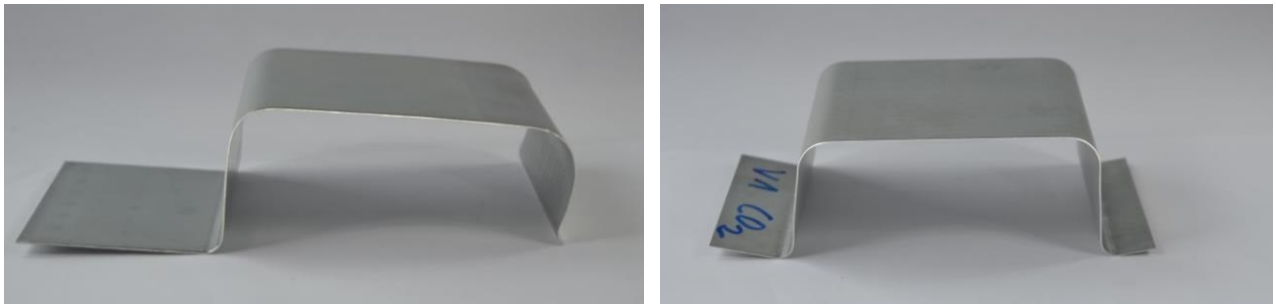

Fig. 44: Deep drawn U-profiles without try-out of tool: left with conventional lubrication, right with $CO_2$ lubrication.

Thus, this result confirms the low friction values determined in the strip drawing test when using $CO_2$ as a lubricant. Good results are achieved even with a tool without spotted blank holder surface and uneven contact conditions. This confirms the outstanding potential of the new approach, which not only seems to allow an equivalent substitution of mineral oil-based lubricants, but even an improvement of the tribological system in sheet metal forming.

## 7 Feasibility studies on the novel tribo-system using rectangular cup geometry

In order to prove the feasibility and process stability of the novel tribo-system using volatile lubricants for dry forming, this technology was applied for the deep drawing process of a rectangular cup geometry. For this purpose, more than 250 micro holes were laser-drilled into the active tool surfaces of the die and the blank holder in order to supply the lubricant (see Fig. 45). In the following subchapters, the design and function of the manufactured tool as well as the test results obtained are described in detail.

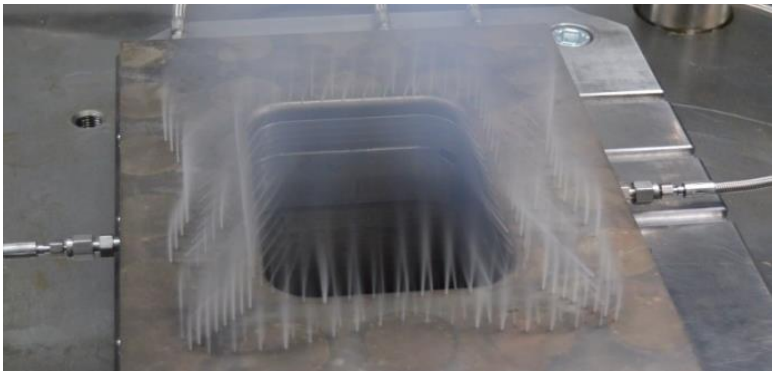

Fig. 45: Drawing die of rectangular cup tool (first version) with free flow out of $CO_2$ through laser drilled micro holes. [27]

### 7.1 Tool design and experimental set-up for dry deep drawing process of rectangular cups

The basic structure of the tool periphery also corresponds to the structure already presented from the U-profile investigations for the implementation of a rectangular cup. The same control of the media supply was used. However, this was adapted and extended for the new geometry, as the number of media supply channels for the rectangular cup has increased.

In order to reduce the drilling depth for the laser process without reducing the tool strength a segmented tool design was chosen (see Fig. 46). The base plate contains the holes for the media supply and a sealing to avoid an uncontrolled flow out between the plates while the upper plate contains different supply channels and laser-drilled micro holes. The position of the supply channels determines the location of micro holes. In order to avoid a free flow out of the media through the micro holes at the end of the forming process the position of the supply channels was optimized using a sheet metal forming simulation of the blank draw-in. As a result, one ring channel was integrated next to the die radius and four additional channels were arranged with regard to the blank draw-in. Each supply channel can be controlled separately by a valve to stop free flow out of media during deep drawing.

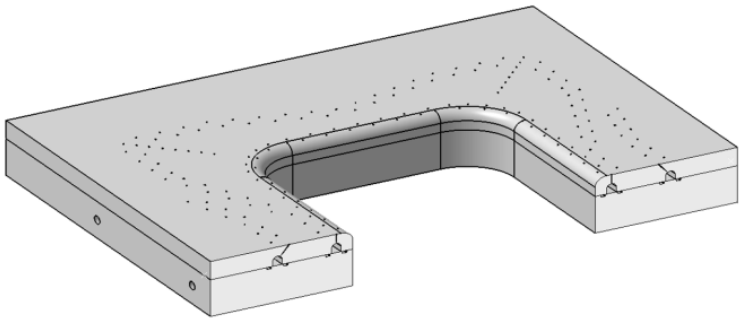

Fig. 46: Cross section through the segmented die of the forming tool of the rectangular cups. Supply channel on left, right side and draw-in radius supply channel can be seen in section area. [27]

One row of micro holes was laser-drilled perpendicular into each supply channel having a depth of 5 mm and one row was incorporated by an angle of 35° and a length of around 7 mm in each supply channel. Additional micro holes were placed in the die radius area. In total, 154 micro holes were distributed over the tool surface of the die. For the blank holder, the same design was chosen though without radius. Here, 100 micro holes were drilled into the tool.

### 7.2 Cooling Effect due to the application of volatile media

The relaxation of $CO_2$ and $N_2$ when flowing out of the micro holes causes a cooling effect on the sheet surface, which is known as Joule-Thomson effect. In order to analyse this effect more detailed, the temperatures of the sheet metal surfaces were measured visually after each deep drawing test using a thermal camera.

| | no lubricant | ZO3368 | $N_2$ | | $CO_2$ |
|---|---|---|---|---|---|
| | - | 1,5 g/m² | 60 bar | 100 bar | ~ 60 bar |
| | 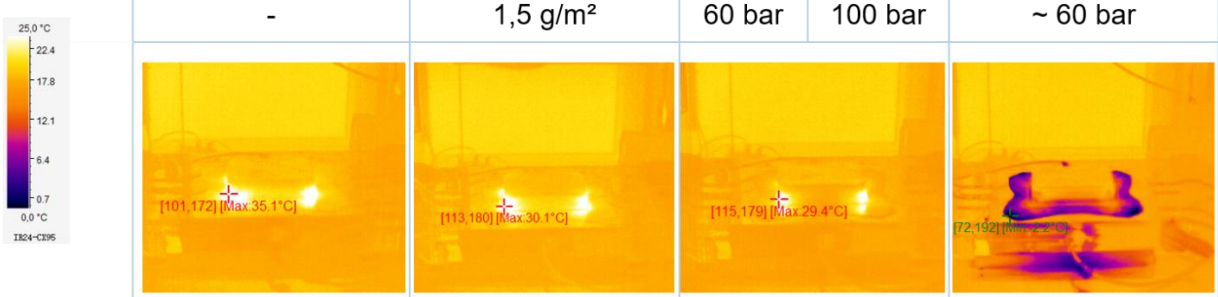 | | | | |
| Results: | Cracks | Good Part (GP) | GP | GP | GP |
| Max. T. [°C] | 35,1 | 30,1 | 33,8 | 29,4 | 19,8 |
| Min. T. [°C] | 18,4 | 18,3 | 17,6 | 17,2 | -2,2 |
| Ø T. [°C] | 21,5 | 21,0 | 20,7 | 19,6 | 13,6 |

(Drawing depth 35 mm und blank holder force 275 kN)

Fig. 47: Measured temperature on the sheet surface after deep drawing using no lubricant, conv. lubricant *ZO3368*, $N_2$ and $CO_2$.

Fig. 47 shows the temperatures visually measured after deep drawing of rectangular cups using no lubrication, conventional mineral oil lubricant *ZO3368* and when using nitrogen and liquid carbon dioxide as lubricant. In each process, a rectangular cup having a drawing depth of 35 mm was produced using a blank holder force of 275 kN. The maximum measured temperature (29.4°C) after deep drawing using nitrogen is almost similar to the sheet temperature when using mineral oil-based lubricants (30.1°C). The heating in the corner of the cup is caused by dissipating forming energy and friction heat. By contrast, liquid $CO_2$ as temporally acting lubricant reduces the sheet temperature in the flange area down to -2.2°C. Compared to the first deep drawing experiments using a U-profile geometry [13], a cooling effect of only a few degrees Celsius were measured. The cooling effect merges much more significantly when deep drawing the rectangular cup. Additional to that the control of valves also plays an important role. Finding the right timing to switch on and off the flow of media appear more complex for the drawing process of a rectangular cup having curved arrangements of micro hole positions onto the tool surface and more complex draw-in compared to previous drawn part as described.

Another reason might be given by effect of changing flange thickness during drawing counteracting to local blank holder force. Small gaps between the tool and the sheet induced by small wrinkles of 1st order can occur supporting the flow out of the $CO_2$ and therefore the cooling of the sheet due to high velocity of media. According to these results, the flow control and also the position of micro holes have to be optimised in further research work in order to reduce observed extreme cooling of the sheet. This cooling effect might be actively used to reduce heating in drawing processes, in which heating of parts due to friction heat and dissipating forming energy is undesirable.

### 7.3 Process window

In order to compare the process stability of the new tribo-system with a conventional tribo-system using mineral oil as lubricant, process windows were determined for each of the tribo-systems. Therefore, the crack and wrinkle limits were determined as a function of the drawing depth for each of the systems by setting different blank holder forces. If the blank holder force was too small, wrinkles of 1st type occurred in the component flange. If the blank holder force was too high, the part cracked at the punch radius. Within these limits, good parts could be obtained. The comparison of the working diagrams shown in Fig. 48 reveals a significant improvement in process stability, when using volatile media as lubricant substitute. With both $N_2$ and $CO_2$, a very high increase in the upper crack limit (up to 250%) can be achieved compared to conventional mineral oil lubrication. Also the maximum achievable drawing depth reaches a much higher value than with mineral oil. The maximum drawing depth could not yet be determined, as the maximum limit of the drawing depth of the tool used was reached at 57.5 mm. However, a slight increase of the wrinkling limit by approx. 100 kN to 150 kN should not be neglected. Nevertheless, this increase is much smaller than the increase of the crack limit, which leads to a very remarkable improvement of the process stability.

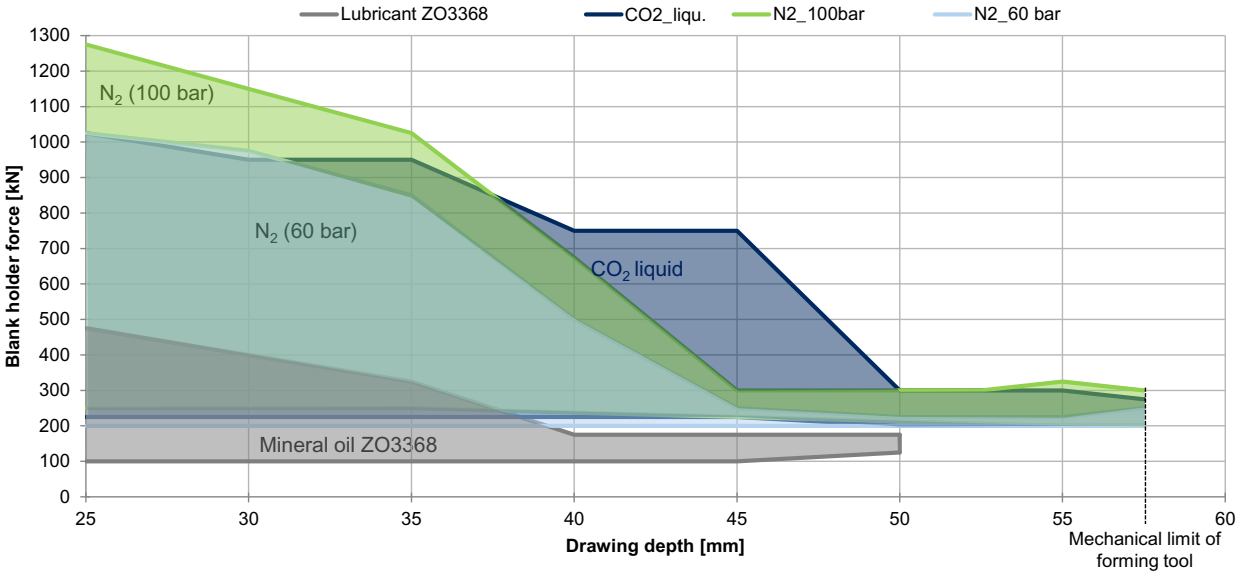


Fig. 48: Process window of the different tribo-systems: mineral oil, $N_2$ at 60 bar, $CO_2$, liquid and $N_2$ at 100 bar. According to [27].

## 8 Outlook

### 8.1 Chemical analysis of the sheet metal surface

To investigate the chemical impact of the lubrication media on the tool steel XPS measurements were made. The tool steel (1.2379) was fractured under different gaseous environments (air, $N_2$, $CO_2$) at different temperature levels. Subsequently the samples were directly tested on chemical reactions or changes in the chemical composition of the surface [25].Though, so far, no investigation of the sheet metal was made. To check the sheet metal for chemical changes during the deep drawing process, while lubricated with different volatile lubrication media, further investigations are planned. Therefore, different sheet metals as well as various gases will be checked.

## 8.2 Endurance investigations on dry deep drawing processes using rectangular cup tool

Main aim of the endurance testing using an improved version of the rectangular cup tool are the proof of the dry forming process stability even under near-series conditions and investigations on the wear behaviour. The process automation has been already built up, where rectangular cups can be deep drawn straight of the coil using a cutting operation. In addition, a numbering embossing unit is integrated into the tool to mark all drawn components with an individual number, which also corresponds to the files of the sensor signals measured for each drawn cup.

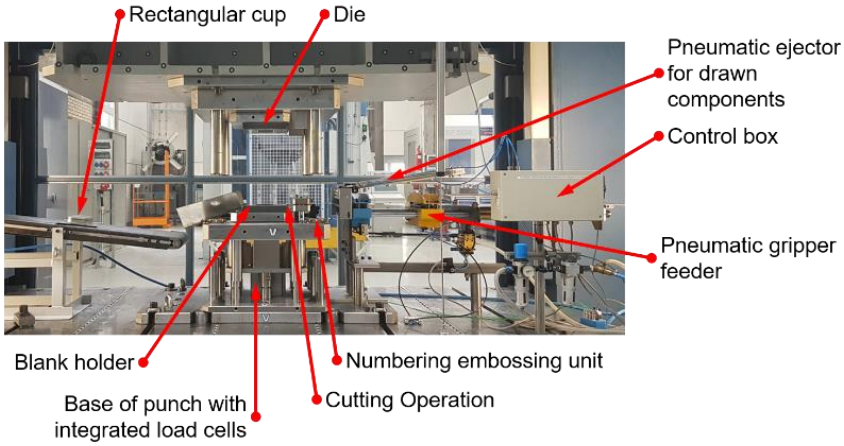


Fig. 49: Process automation for deep drawing of rectangular cups under near series conditions.

Findings obtained this way will show to what extent the new tribological system is suitable for a series application or whether any further optimisation is required. The endurance investigations will be carried out and evaluated in the 2nd quarter of this year.

## 8.3 Laser-drilling of the improved forming tool

In order to enable endurance testing for the production of rectangular cups, an improved version of the forming tool will be laser-drilled using the IFSW kW-ps laser to increase productivity and improve the accuracy of the micro hole positioning by using a multi-axis CNC laser beam guidance system. Further research will investigate the influence of dynamic longitudinal beam displacement on micro hole geometry during the drilling process.


## Acknowledgements

The scientific investigations of this research are funded by the German Research Foundation (DFG) within the priority program SPP 1676 Dry Metal Forming - Sustainable Production by Dry Processing in Metal Forming. We thank the German Research Foundation (DFG) for the funding of this research projects (Li 1556/49-2, GR 3172/21-2, TO 211/3-2, HI 1397/6-1). More Information can be found at www.trockenumformen.de.


## References


[1] H. Mishina, “Atmospheric characteristics in friction and wear of metals,” *Wear*, vol. 152, no. 1, pp. 99–110, 1992.

[2] X. Wu, P. Cong, H. Nanao, I. Minami, and S. Mori, “Tribological Behaviors of 52100 Steel in Carbon Dioxide Atmosphere,” *Tribol. Lett.*, vol. 17, no. 4, pp. 925–930, 2004.

[3] F. Vollertsen and F. Schmidt, “Dry metal forming: Definition, chances and challenges,” *Int. J. Precis. Eng. Manuf. - Green Technol.*, vol. 1, no. 1, pp. 59–62, 2014.

[4] M. Liewald *et al.*, “Tribosysteme für die Kaltumformung auf der Basis von flüchtigen Schmiermedien und laserstrukturierten Oberflächen - 2,” *Dry Met. Form. OAJ FMT 1*, vol. 1, pp. 113–120, 2015.

[5] L. Böswirth, S. Bschorer, and T. Buck, *Technische Strömungslehre: Lehr- und Übungsbuch*, 10., übera.

Wiesbaden: Springer Vieweg, 2014.

[6] E. Zahedi *et al.*, “Lubricant-free deep drawing using CO2 and N2 as volatile media injected through laser-drilled microholes,” *MATEC Web Conf.*, vol. 190, no. 9, p. 14007, 2018.

[7] M. Liewald, G. E. M. Tovar, C. Woerz, and G. Umlauf, “Tribological Conditions Using CO2 as Volatile Lubricant in Dry Metal Forming,” *Int. J. Precis. Eng. Manuf. Technol.*, vol. 11, no. 3, p. 361, 2019.

[8] ChemicaLogic Corporation, Ed., “Carbon Dioxide Phase Diagram.” .

[9] S. Döring, S. Richter, A. Tünnermann, and S. Nolte, “Evolution of hole depth and shape in ultrashort pulse deep drilling in silicon,” *Appl. Phys.*, vol. A 105, pp. 69–74, 2011.

[10] J. P. Negel *et al.*, “1.1 kW average output power from a thin-disk multipass amplifier for ultrashort laser pulses,” *Opt. Lett.*, vol. 38, pp. 5442–5445, 2013.

[11] R. Weber *et al.*, “Heat accumulation during pulsed laser materials processing,” *Opt. Express*, vol. 22, no. 9, pp. 11312–11324, 2014.

[12] D. J. Förster, R. Weber, and T. Graf, “Residual heat during ultrashort laser drilling of metals,” in *Proceedings of LPM 2017 - the 18th International Symposium on Laser Precision Microfabri-cation*, 2017.

[13] C. Wörz, E. Zahedi, G. Umlauf, M. Liewald, R. Weber, and G. E. M. Tovar, “Tiefziehen eines U-Profils mit flüchtigen Medien als Schmierstoffersatz,” *Dry Met. Form. OAJ FMT 3*, vol. 3, 2017.

[14] E. Zahedi *et al.*, “Lubricant-free deep drawing using CO2 and N2 as volatile media injected through laser-drilled microholes,” *Manuf. Rev.*, vol. 6, p. 11, May 2019.

[15] D. J. Förster, R. Weber, D. Holder, and T. Graf, “Estimation of the depth limit for percussion drilling with picosecond laser pulses,” *Opt. Express*, vol. 26, pp. 11546–11552, 2018.

[16] D. Breitling, A. Ruf, and F. Dausinger, “Fundamental aspects in machining of metals with short and ultrashort laser pulses,” in *Proc. SPIE 5339, Photon Processing in Microelectronics and Photonics III*, 2004, p. 15.

[17] S. Döring, S. Richter, S. Nolte, and A. Tünnermann, “In situ imaging of hole shape evolution in ultrashort pulse laser drilling,” *Opt. Express*, vol. 18 (19), pp. 20395–20400, 2010.

[18] S. Döring, “Analysis of the Hole Shape Evolution in Ultrashort Pulse Laser Drilling,” Cuvillier Verlag, 2014.

[19] A. Michalowski, “Untersuchungen zur Mikrobearbeitung von Stahl mit ultrakurzen Laserpulsen,” 2014.

[20] M. Henn, G. Reichardt, R. Weber, T. Graf, and M. Liewald, “Dry metal forming using volatile lubricants injected into the forming tool through flow-optimized, laser-drilled microholes,” *to be Publ. JOM (The J. Miner. Met. Mater. Soc. - TMS)*, 2020.

[21] M. Singer, M. Liewald, and A. Feuer, *Development of a new ecological lubrication system for sheet metal forming based on CO2 in liquid*, vol. 651–653. 2015.

[22] M. Liewald *et al.*, “Tribosysteme für die Kaltumformung auf der Basis von flüchtigen Schmiermedien und laserstrukturierten Oberflächen,” *Dry Met. Form. OAJ FMT 1*, vol. 1, pp. 22–33, 2015.

[23] G. Umlauf *et al.*, “Grundlagenuntersuchungen zur Herstellung von Lasermikrobohrungen in Stahl und dem Ausströmverhalten von CO2 als Trockenschmiermedium,” *Dry Met. Form. OAJ FMT 2*, vol. 2, pp. 18–24, 2016.

[24] P. W. Atkins, J. de Paula, and J. Keeler, *Atkins’ physical chemistry*, Eleventh e. Oxford and New York: Oxford University Press, 2018.

[25] A. Almohallami *et al.*, “How dry is dry ? - A critical analysis of surface conditions used in dry metal forming,” *Dry Met. Form. OAJ FMT 3*, vol. 3, pp. 90–94, 2017.

[26] C. Woerz, M. Liewald, and M. Singer, “Investigation of Tribological Conditions in the Strip Drawing

Test Using Liquid CO2 and N2 as a Volatile Lubricant," in *7th International Conference on Tribology in Manufacturing Processes (ICTMP)*, 2016, pp. 140–148.

[27] C. Wörz, G. Reichardt, M. Liewald, E. Zahedi, and R. Weber, "Dry deep drawing of a rectangular cup assisted by volatile media injected from laser-drilled microholes," *Dry Met. Form. OAJ FMT 4*, vol. 4, pp. 1–8, 2018.

[28] H. Hasselbruch, M. Herrmann, A. Mehner, H.-W. Zoch, B. Kuhfuss, "Development, characterization and testing of tungsten doped DLC coatings for dry rotary swaging," *MATEC Web Conf.*, vol. 21, pp. 1–7, 2015.

[29] G. Umlauf, H. Hasselbruch, J. H. Henze, J. Barz, and A. Mehner, "A new approach for dry metal forming : CO2 as volatile lubrication in combination with hard and low friction coatings," in *5th International Conference on New Forming Technology (ICNFT 2018)*, 2018, vol. 190, pp. 1–7.

[30] G. Reichardt and M. Liewald, "Friction Conditions on Deep-Drawing Tool Radii When Using Volatile Media as Lubrication Substitute," in *TMS 2019 - Supplemental Proceedings*, 2019, pp. 1603–1613.

[31] A. Papaioanu, "Einsatz eines neuartigen Verfahrens zum kombinierten Recken und Tiefziehen von Außenhauptbeplankungen aus Feinblech," University of Stuttgart, 2016.